12-2022

First-Principles Study of Doping Effects on Ferroelectricity and on Rashba Spin Splitting

Zegnet Yimer Muhammed
University of Arkansas, Fayetteville

First-Principles Study of Doping Effects on Ferroelectricity and on Rashba Spin Splitting

This dissertation is submitted in partial fulfillment
of the requirements for the degree of
Doctor of Philosophy in Physics

by

Zegnet Yimer Muhammed
Bahir Dar University
Bachelor of Education in Physics Minor Mathematics, 2006
International Center for Theoretical Physics
Postgraduate Diploma in Basic Physics, 2010
University of Texas El Paso
Master of Science in Physics, 2015

December 2022
University of Arkansas

This dissertation is approved for recommendation to the Graduate Council.

Huaxiang Fu, Ph.D.
Dissertation Director

Laurent Bellaiche, Ph.D.
Committee Member

Reeta Vyas, Ph.D.
Committee Member

Abstract

In this dissertation, we have thoroughly studied the effect of chemical and charge doping on ferroelectrics ($PbTiO_3$ and $BaTiO_3$) and Rashba type semiconductor (BiTeI). In the first project, We investigate the polar instability and soft modes in electron-doped $PbTiO_3$ using linear-response density functional calculations. Because, metallicity and ferroelectric-like polar distortion are mutually non-compatible, and their coexistence in the same system is an intriguing subject of fundamental interest in the field of structure phase transition. However, it is unclear what mechanism may extend the limit of metallicity that allows polar distortion. We find that ferroelectric instability can remarkably sustain up to an electron concentration of n_e=0.7 per unit cell, which is beyond the limit that causes the polar catastrophe in $LaAlO_3/SrTiO_3$. Our study further reveals two unusual discoveries: (i) Electron doping can turn non-soft mode into soft mode, which leads to different microscopic mechanism for ferroelectricity when system is strongly metallic; (ii) The frequency change $\Delta\omega/\Delta n_e$ is surprisingly flat at large n_e, which is pivotal for the persistence of soft mode and polar distortion at high metallicity. We also provide an interesting physical origin—which is caused by the strong mode-mode interaction—to explain these phenomena, and the finding of this origin may further extend the limit where metallicity and polar distortion coexist. In the second project, after we understood the existence of polar-metal characteristics in $PbTiO_3$ under electron doping, we extend our study to a more complex system of supercell $PbTiO_3$ under chemical doping and the application of biaxial compressive strain to find room temperature polar-metal. Polar metals offer a wide range of useful properties in superconductivity, magnetoelectricity, photovoltaics, and mutli-ferroic sensors. The realization of a room temperature polar metals would be an ideal candidate for such versatile applications. Hence, using liner-response density functional calculations, we have investigated Nb-doped $PbTiO_3$, which is under four different biaxial compressive strains (η=0%, -1%, -2%, and -3%) to alter the minimum energy of its polar mode ($A_{2u}(TO_1)$). We find from the total density of states of

-2% biaxially strained Nb-doped $PbTiO_3$ that the frequencies of most phonon modes are less than 300 cm^{-1}. We also find that the extra electron acquired due to Nb-doping is localized and form small polarons around Nb site, which can be thermally actuated into a conduction state. This electron partially screens out the internal dipole moment existed in pure (without Nb-doping) $PbTiO_3$, and preserves the ferroelectric instability. The double well potential depth of $A_{2u}(TO_1)$ display stability under room temperature condition ($K_BT \sim 25$ meV) for η=-2% and η=-3%, because the depth of the potential well for these two strains are -29.51 and -39.56 meV, respectively. However, the depth of the potential well of $A_{2u}(TO_1)$ for unstrained (η=0%) Nb-doped $PbTiO_3$ is -0.095 meV, which is unstable at this condition. We therefore demonstrated that metallic Nb-doped $PbTiO_3$ can be transformed into polar metal by the application of biaxial compressive strain. As a result, strain play a prominent role to tune the physical and chemical properties of polar metals in addition to doping. Finally, in the third project, we investigate the effect of electron and hole doping on the spin-orbit interaction and electron-phonon coupling constant of BiTeI. The spin-splitting of bands by spin-orbit interaction (SOI) in systems that lack inversion symmetry have paramount importance in spin-polarized field effect transistor, magnetoelectric effect, Edelstein effect and spin Hall effect. We have performed first principle calculation to study the effect of charge doping (electron and hole) on the SOI and electron-phonon coupling constant (λ) of BiTeI. The Rashba parameter is tuned up to a maximum value of 7.46 and 6.32 eV$\mathring{A}$ for the valance and conduction bands, respectively. The valance band Rashba parameter is so far the highest we have recognized in any work. λ of BiTeI is 0.46, and this value is almost the same as that of Al and Mo. However, the critical temperature (T_C) of BiTeI in this study is 0.7 K, which is very small for practical application.

Acknowledgements

First and foremost, I would like to thank sincerely my advisor Prof. Huaxiang Fu for his invaluable and excellent guidance. He is among one of the best scholars that I had taken a course with, and that is why I have decided to work with him since then. Not only he always encouraged me to think outside of the box and become a better scientist, but also he cares the most. Moreover, he is very enthusiastic and sincere in what he does. I am very grateful for his unconditional support, compassion, and responsiveness; I have learnt a lot from him. I would also like to thank the dissertation committee members: Prof. Laurent Bellaiche and Prof. Reeta Vyas. This dissertation would have not been possible without their critics and constructive ideas. Prof. Laurent Bellaiche's kindness, humbleness, and professionalism are the most aspiring qualities that I would like to follow as a physicist. I am forever indebt for his unwavering help and discussion pertaining to physics and soccer. I guess he would have been a soccer player if he had not chosen to follow academia. Thank you Prof. Reeta Vyas for your encouragement and advice to apply for the physics graduate program at the University of Arkansas, Fayetteville while I was looking at different Universities to attend graduate school. Furthermore, your critical comments and questions as an advising committee helped me immensely to improve presentation skills and understand physics well. I would like to acknowledge Prof. Tunna Baruah and Rajendra Zope from the University of Texas El Paso (UTEP) with whom I did my master degree, and they have been very supportive even after I left UTEP.

I would like to thank my dear friends here at the physics department and Lewis soccer field for the joy and friendship they brought to make life as simple as possible. Finally, I would like to thank the physics faculty and staff for their day to day activities and support to make the teaching-learning process smooth.

Dedication

For my beloved sister, mother, and grandmother.

Contents

List of Tables

List of Figures

List of Published Papers

Chapters 1 is published as follows and copyright information can be found in Appendix.

- (Chapter 1) Yimer, Z. and Fu H. (2020). Origin of the persistence of soft modes in metallic ferroelectrics. Physical Review B, 101(17), 174105.

1 Origin of the persistence of soft modes in metallic ferroelectrics

1.1 Introduction

1.1.1 Polar Metals

Coexistence of metallicity and ferroelectric-like polar distortion, namely that a solid is simultaneously metallic and polar as suggested first by Anderson and Blount [1], is an intriguing phenomenon of fundamental interest, since the two properties are mutually incompatible and should not occur in the same system [2]. For decades, the long-range Coulomb interaction was known to favor ferroelectricity (FE) by causing atoms to move off-center and thus developing polarization [3–6]. On the other hand, the mobile carriers (electrons or holes) existing in *metallic* materials tend to annihilate (by charge screening) the asymmetric charge distribution and electric dipole if ferroelectricity is to persist. Consequently polar metals with simultaneous occurrence of both metallicity and polar distortion were conceived to be paradoxical and interesting.

Technologically, the peculiar coexistence offers an interesting possibility of using conductivity and polarity as two different routes to tune material properties. Metals exhibit good transport such as superconductivity [7] and quantum Hall effects [8], while ferroelectrics provide other superior properties [9], such as ultrahigh electromechanical response [10, 11], interesting morphotropic phase boundary [12, 13], exceptional dielectric coefficient [14], large proximity effect [15], unusual phase transitions [16, 17], and strong coupling between rotation and polarization [18–21]. The intriguing interplay between two drastically different fields is largely unknown. Polar metals may also replace normal metal electrodes for better functionality and enhanced performance [22]. Furthermore, the presence of polar axis in polar metals breaks the inversion symmetry and introduces a non-vanishing spin-orbit coupling [23], which causes detectable band splitting in the natural gyrotropy and spin susceptibility of superconductors $CePt_3Si$, UIr, and KOs_2O_6 [24, 25]. Moreover, electrical current in polar

metals may induce a spin magnetization proportional to $\vec{P} \times \vec{J}$ (where $\vec{P}$ is the unit vector along the polar axis and $\vec{J}$ is the current density), which may lead to novel magnetoelectric effect [25] and double circular refraction by Faraday and Kerr rotations [26].

Polar metals are realized either by undoped nature materials [2, 27–30], or by doping ferroelectrics with conducting electrons [31, 32]. Shi *et al.* demonstrated experimentally that *metallic* $LiOsO_3$ undergoes at 140K a *ferroelectric* phase transition from the centrosymmetric $R\bar{3}c$ to non-centrosymmetric R3c structure [27], which supports the existence of polar metals. Polar axis also occurs in metal $SrCaRu_2O_6$ [33]. Although the mechanism of polar metals is still largely unknown, the existing studies point to the possibility that the short-range interaction, in addition to the long-range interaction, may stabilize ferroelectricity [28–32].

Many profound issues on polar metals remain to be understood. Questions of fundamental relevance are: (i) To what extent can the ferroelectric instability be sustained in metals, in terms of the concentration of conducting electrons? (ii) What is the mechanism for causing ferroelectric instability when metallicity is strong? (iii) Do soft modes at *high* conductivity resemble those at *low* conductivity? Could it be possible that they may drastically differ? (iv) How do the *non-soft* modes respond to metallicity besides the soft modes? Answers to these questions would not only provide a better understanding of polar distortions in metals, but also open new prospects for designing polar metals.

In this project we study how, and why, polar instability may exist when metallicity is particularly strong, by investigating the structural instability and soft modes in centrosymmetric $PbTiO_3$ under electron doping. By carefully mapping out the evolution of soft modes as a function of electron doping, we are able to determine accurately how each mode is formed and evolves when metallicity is changing. We find that ferroelectric instability persists robustly up to an unusually-high electron-doping concentration (n_e) of $0.7e$ per unit cell. Furthermore, the microscopic mechanism of forming FE under high metallicity is demonstrated to differ drastically from that under low metallicity. Moreover, we provide an interesting and previously less explored origin, caused by strong mode-mode interaction, to explain the

unusual persistence of polar instability under high metallicity.

1.2 Methods

1.2.1 Density functional theory (DFT)

Density functional theory (DFT) within the local-density approximation [34, 35], as implemented in Quantum Espresso [36, 37], is used to determine total energy, atomic force, and optimal structure. Norm-conserving pseudopotentials are used [38]. Semicore $3s$ and $3p$ states of Ti are treated as valence states to ensure better accuracy [39, 40]. The energy cutoff for the plane-wave expansion of singleparticle states is 90 Ry. 6×6×6 Monkhorst-Pack k-mesh is used.

1.2.2 Density functional perturbation theory (DFPT)

The linear-response density functional perturbation theory (DFPT) is employed to compute the phonon frequencies and eigenvectors [41–43]. When atoms vibrate, the shifts of atoms induce a deformation potential $\Delta V(\mathbf{r})$ of bare ions, which is treated as perturbation. The linear response of electron state $\Delta\psi_n(\mathbf{r})$ is computed [41, 42] by solving the Sternheimer equation:

$$(H_{scf} - \varepsilon_n)|\Delta\psi_n\rangle = -(\Delta V_{scf} - \Delta\varepsilon_n)|\psi_n\rangle \tag{1.1}$$

where H_{scf} is the Kohn-Sham Hamiltonian, ε_n the eigenvalue of H_{scf}, $\Delta V_{scf}(\mathbf{r}) = \Delta V(\mathbf{r}) + e\int \frac{\Delta n(\mathbf{r}\prime)}{|\mathbf{r}-\mathbf{r}\prime|}\,\mathrm{d}\mathbf{r}\prime + \left.\frac{dv_{xc}(n)}{dn}\right|_{n=n(\mathbf{r})} \Delta n(\mathbf{r})$ the first-order correction to the $V_{scf}(\mathbf{r})$ potential, and $\Delta\varepsilon_n{=}\langle\psi_n|\Delta V_{scf}(\mathbf{r})|\psi_n\rangle$ is the first-order correction to eigenvalue ε_n. The variation of electron state $\Delta\psi_n(\mathbf{r})$ is computed by solving the Sternheimer equation [44].

For ferroelectric (i.e., non-centrosymmetric) $PbTiO_3$ with P4mm symmetry, our structural optimization yields an inplane lattice constant a=3.85 Å and tetragonality c/a=1.047. These values are in agreement with previous results [45] of a=3.87 Å and c/a=1.040. Our calculated phonon frequencies in ferroelectric $PbTiO_3$ are 81 cm^{-1} for E(TO_1) mode and 616 cm^{-1} for A_1(TO_3) mode, which compare well with other computed values of 82 cm^{-1} and

623 cm^{-1}, respectively [46]. These results show that our calculations are reliable.

For centrosymmetric $PbTiO_3$, atoms are placed at their high-symmetric positions in the tetragonal lattice so that the solid exhibits ferroelectric instability. Different amount of electron per unit cell, denoted as n_e, is added to the system which now becomes metallic. The doped electrons will mainly occupy the Ti orbitals and change the charge state of Ti atoms from Ti^{4+} to $Ti^{(4-\delta)+}$ because the electron states at the bottom of the conduction bands are largely Ti $3d$ orbitals. We perform electron doping by changing the number of electrons in the system while adding the charge-compensating jellium background in order to avoid the diverging Coulomb energy in a charged periodic system [47]. The dipole correction is small and is not considered, since this correction is inversely proportional to the static dielectric constant of the solid and since the static dielectric constant is large in ferroelectric materials (e.g., about 2000 at low temperature in $BaTiO_3$). We investigate by DFPT the phonon frequencies and eigenvectors when the system is under different doping concentration n_e.

1.3 Results and Discussions

1.3.1 Persistency of soft modes at high n_e

According to the group theory [48], the normal modes in centrosymmetric $PbTiO_3$ are $5E_u \bigoplus 4A_{2u} \bigoplus B_{2u}$. E_u modes are doubly degenerate and vibrate along the ab plane of perovskites, while A_{2u} and B_{2u} modes are singly degenerate and vibrate along the c axis.

The calculated phonon frequencies for centrosymmetric $PbTiO_3$ under different doping concentration n_e (i.e., the number of doped electrons per 5-atom unit cell) are shown in the 4th to 6th columns in Table 1.1. For undoped $PbTiO_3$ (n_e=0), it is no surprise that soft modes should occur since centrosymmetric $PbTiO_3$ is not stable [49]. Indeed, for n_e=0, our results in Table 1.1 show that the low-frequency modes $A_{2u}(TO_1)$ and $E_u(TO_1)$ are soft with imaginary frequencies of -241 and -135 cm^{-1}, respectively (see the 4th column in Table 1.1).

Interestingly, we find that, when doping concentration is increased to n_e=0.6, three (i.e.,

Table 1.1: Phonon frequencies (ω) at Γ point in centrosymmetric $PbTiO_3$ under different doping concentration (n_e) are reported in the 4th to 6th columns. Furthermore, for the undoped case (n_e=0), the mode order, mode label, and slope $\Delta\omega/\Delta n_e$ of frequency change (in cm^{-1}) are listed in the 1st, 2nd, and 3rd columns, respectively. Imaginary frequencies of soft modes are given as negative values. Three trivial acoustic modes with zero frequency are not included.

n_e=0				n_e=0.3	n_e=0.6
Order	Mode label	$\Delta\omega/\Delta n_e$	ω (cm^{-1})	ω (cm^{-1})	ω (cm^{-1})
1	$A_{2u}(TO_1)$	690.6	-241	-59	-39
2,3	$E_u(TO_1)$	617.9	-135	-50	-45
7	$A_{2u}(TO_2)$	141.9	83	205	247
8,9	$E_u(TO_2)$	456.2	111	233	270
10	B_{2u}	150.8	199	227	310
11,12	$E_u(TO_3)$	32.2	244	276	334
13	$A_{2u}(TO_3)$	60.5	441	464	479
14,15	$E_u(TO_4)$	130.8	497	554	587

more than one) modes in the sixth column of Table 1.1 remain soft with imaginary frequencies. Note that n_e=0.6 corresponds to a doped-electron concentration of $\sim 10^{28}$ electrons/m^3, which is exceptionally high in normal semiconductors [50]. Results in Table 1.1 thus demonstrate that soft modes exist despite strong metallicity, which is rather remarkable. To further illustrate how strong the metallicity is in $PbTiO_3$ with n_e=0.6 per unit cell, we note that this n_e value exceeds the charge transfer of n_e=0.5 per unit cell from $LaAlO_3$ to $SrTiO_3$, and the charge transfer of n_e=0.5 in the latter case is sufficient to cause a strong metal/insulator transition in the $LaAlO_3/SrTiO_3$ system [51]. Our calculations thus reveal that ferroelectric soft modes in $PbTiO_3$ can persist under strong metallicity.

The existence of soft modes at n_e=0.6 is not accidental, and it also occurs at another concentration n_e=0.3 (the fifth column in Table 1.1). The persistence of ferroelectric soft modes at different levels of electron doping unambiguously proves that polar metals indeed exist.

1.3.2 Unusual behaviors of soft modes in doped $PbTiO_3$

To obtain a microscopic understanding of polar distortion in metallic systems, we now examine the phonon eigenvector of the lowest-frequency soft mode (LFSM), which is shown

in Figure 1.1 for different doping concentrations. For n_e=0 in Figure 1.1(a), the LFSM mainly originates from the opposite displacements of Ti and O atoms, which is a Slater mode [52, 53]. Pb atoms also have a sizable contribution in Figure 1.1(a).

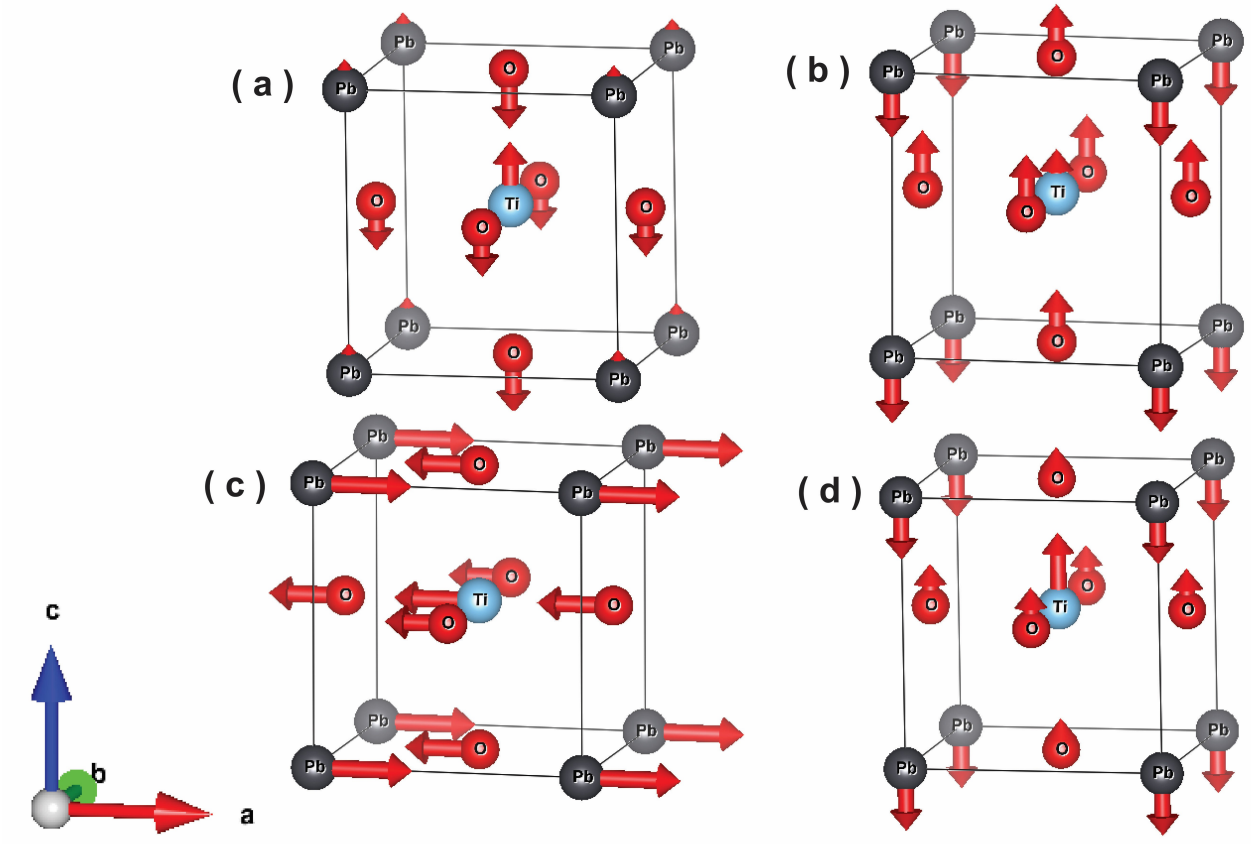

Figure 1.1: Phonon eigenvector of the lowest-frequency soft mode (LFSM) at different n_e: (a) n_e=0.0; (b) n_e=0.3; (c) n_e=0.6. The phonon eigenvector of the non-soft $A_{2u}(TO_2)$ mode at n_e=0 is shown in (d). Arrow and its length indicate the vibration direction and amplitude, respectively.

As n_e is increased to 0.3, we find that the LFSM in Figure 1.1(b) is intriguingly different from the one in Figure 1.1(a): (i) For the LFSM in Figure 1.1(b), Ti and O atoms are *not* moving along opposite directions, and instead they move along the same direction. The LFSM at n_e=0.3 thus becomes a Last mode [54], not a Slater mode as in Figure 1.1(a). Figure 1.1(b) reveals that the Ti-O opposite displacement is no longer responsible for the

ferroelectricity in $PbTiO_3$ at n_e=0.3. (ii) In Figure 1.1(b), the Pb contribution is drastically enhanced, and the Pb and O atoms are displaced along opposite directions. Therefore ferroelectric instability in $PbTiO_3$ polar metal at n_e=0.3 originates mainly from the relative motion of Pb and O atoms, unlike in undoped $PbTiO_3$. We thus discover that ferroelectricity in undoped and doped $PbTiO_3$ has different *microscopic* origins.

When n_e is further increased to 0.6, the LFSM in Figure 1.1(c) is also unexpected. Unlike either Figure 1.1(a) or Figure 1.1(b) (where atoms vibrate along the c axis), the LFSM at n_e=0.6 now vibrates on the ab plane, suggesting that ferroelectricity occurs within the inplane direction, caused by high carrier concentration. To further confirm that the LFSM at n_e=0.6 in Figure 1.1(c) will indeed cause structural instability, we have performed structural optimization by relaxing the cell shape and atomic positions. We find that the ground state of n_e=0.6 is a monoclinic M_A-like structure where there is a sizable tetragonal distortion. Meanwhile, the Ti atom moves along the ab plane as well as along the c-axis, since soft mode $E_u(TO_1)$ leads to a displacement along the ab plane and another competing soft mode $A_{2u}(TO_1)$ leads to a displacement along the c-axis. Again, the relative displacements of Ti and O atoms cease to be the origin of ferroelectricity since they move along the same direction in Figure 1.1(c). The large and opposite Pb-O displacement in Figure 1.1(c) is the reason responsible for the ferroelectricity. Figure 1.1(b) and Figure 1.1(c) thus reveal that ferroelectric instability in polar metals is rich and interesting, tunable by the concentration of conducting carriers.

1.3.3 Mode evolution and doping-induced frequency change $\Delta\omega/\Delta n_e$

The mode frequencies in Table 1.1 at the three doping concentrations (n_e=0, 0.3, 0.6) are plotted in the inset of Figure 1.2. From the inset it is hard to see how modes at one n_e evolve into modes at another n_e, particularly when several modes are clustered with similar frequencies. Here we use two tactics to solve this evolution problem. First, we perform calculations for more doping concentrations. Second, we utilize a mode-projection method

(which is described below) to determine *quantitatively* the relation among modes at different n_e.

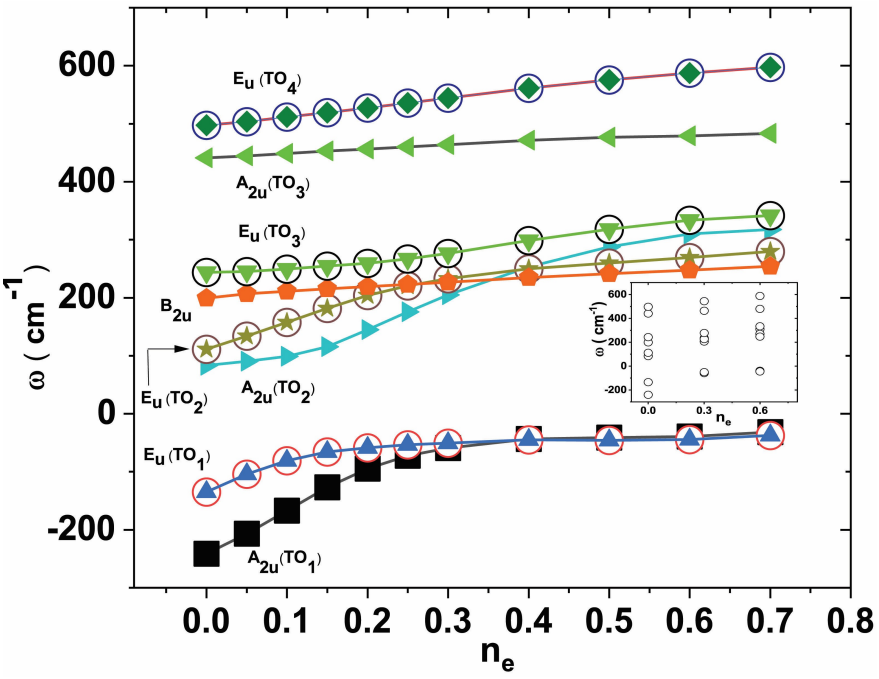

Figure 1.2: Phonon frequencies at Γ point as a function of n_e in electron-doped $PbTiO_3$. Symbols are the results directly obtained from DFPT calculations; lines that depict the mode evolution between different n_e are obtained by mode projection. Labels of normal modes are given near each curve. The inset shows the mode frequencies for three n_e (i.e., 0, 0.3, 0.6) considered in Table 1.1.

Denote the mth zone-center phonon eigenvector at doping concentration n_e as $|\epsilon_m^{i\alpha}(n_e)\rangle$, where i is the atom index and α the direction index. Eigenvector $|\epsilon_m^{i\alpha}(n_e)\rangle$ is related to the phonon displacement $|u_m^{i\alpha}(n_e)\rangle$ by $|\epsilon_m^{i\alpha}(n_e)\rangle = \sqrt{M_i}|u_m^{i\alpha}(n_e)\rangle$, where M_i is the mass of atom i.Since phonon eigenvectors at a given wave vector form a complete basis set, we can thus use the phonon eigenvectors at one doping concentration n_{e1} as bases to expand the phonon eigenvectors at another doping concentration n_{e2},

$$|\epsilon_l^{i\alpha}(n_{e2})\rangle = \sum_m p_{ml}\,|\epsilon_m^{i\alpha}(n_{e1})\rangle\ , \tag{1.2}$$

where p_{ml}=$\sum_{i\alpha}\langle\epsilon_m^{i\alpha}(n_{e1})|\epsilon_l^{i\alpha}(n_{e2})\rangle$. Quantity p_{ml} describes the correlation between mode m at n_{e1} and mode l at n_{e2}, establishing the correspondence among modes at different n_e.

Eq.(1.2) is rigorous since phonon eigenvectors at one doping concentration are complete bases for a given phonon wave vector. This equation does not apply to the force constant matrices because the force constant matrix at one doping concentration does not form a complete basis set. Also, the relation between phonon eigenvectors and force constant matrices cannot be formulated analytically in a simple manner, which makes it hard to apply Eq.(1.2) to the force constant matrices.

The DFPT-calculated phonon frequencies for more doping concentrations are plotted as the symbols in Figure 1.2. We then perform the mode projection and determine the evolution for phonon modes between two neighboring n_e. The evolution is given by the solid lines in Figure 1.2. Determination of the continuous evolution of modes is important, since it allows us (i) to understand the origin of each mode, and (ii) to compute quantitatively how the frequency of a specific mode changes with n_e.

It is interesting to examine how frequency (ω) of individual mode depends on n_e. At a *low* doping concentration when n_e is less than 0.1, we find that frequency ω in Figure 1.2 depends on n_e in a linear manner. The linear slope $\Delta\omega/\Delta n_e$ at n_e=0 is determined and given in the third column in Table 1.1. Table 1.1 shows that (i) soft mode $A_{2u}(TO_1)$ and $E_u(TO_1)$ each has a giant $\Delta\omega/\Delta n_e$, which is 690.6 and 617.9 cm^{-1}, respectively; (ii) Interestingly, some *non-soft* phonons such as modes 8 and 9 [i.e., $E_u(TO_2)$] also demonstrate a surprisingly large slope of 456.2 cm^{-1}, showing that assumption of small $\Delta\omega/\Delta n_e$ for non-soft phonons cannot be justified; (iii) Even for the silent B_{2u} mode (mode 10 in Table 1.1), the slope $\Delta\omega/\Delta n_e$ is nonzero, revealing a broad impact caused by metallicity on lattice vibration. Silent B_{2u} mode involves only the oxygen atoms on the base plane of an oxygen octahedron, where two opposite oxygen atoms move upward along the c-axis while another two oxygen atoms move downward.

Using the $\Delta\omega/\Delta n_e$ slope in Table 1.1, one may estimate the critical doping concentration n_e^c at which a soft mode will disappear. n_e^c is found to be n_e^c=0.35 for soft mode $A_{2u}(TO_1)$. In other words, $A_{2u}(TO_1)$ will no longer be soft after n_e^c=0.35. However, this does not occur

in reality, and as a matter of fact, in the 6th column of Table 1.1, mode $A_{2u}(TO_1)$ continues to be soft at n_e=0.6, which is much larger than n_e^c. This is rather astonishing, and indicates that interesting phenomena must happen at high doping concentration.

Indeed, Figure 1.2 shows that frequency change $\Delta\omega$ at high n_e is completely different from that at low n_e. In particular, the $\Delta\omega/\Delta n_e$ slopes of the two lowest curves [i.e., $A_{2u}(TO_1)$ and $E_u(TO_1)$] in Figure 1.2 are remarkably flat when $n_e \geq$0.3. The flat $\Delta\omega/\Delta n_e$ slope of the soft mode is unusual and interesting for two reasons: (i) Most of the other modes do not have a flat $\Delta\omega/\Delta n_e$ slope at large n_e as shown in Figure 1.2; (ii) The flat $\Delta\omega/\Delta n_e$ slope reveals that increasing n_e does not change significantly the frequency of the soft mode, and thus allows the soft mode to persist at high n_e (which is critical for the persistence of soft mode and polar instability to sustain up to n_e=0.7 in electron-doped $PbTiO_3$). Also, it worths mentioning that the mode sequence (i.e., the ordering of modes according to frequencies) is very different at n_e=0.7 than at n_e=0; for instance, at n_e=0.7, the silent B_{2u} now becomes the lowest non-soft phonon (Figure 1.2).

1.3.4 Origin of the persistence of polar instability in doped $PbTiO_3$

The discoveries of (i) the persistence of soft modes up to a high doping concentration of n_e=0.7, (ii) the unusual alternation of the LFSM in Figure 1.1, and (iii) the drastic change in $\Delta\omega/\Delta n_e$ at low and high metallicity in Figure 1.2, are all interesting. In the following we attempt to find the physical origin explaining these behaviors.

First we intend to provide *quantitative* evidence showing that electron doping (and metallicity) causes a strong mode-mode interaction. For this purpose, we investigate where the LFSM at n_e=0.3 originates from, by projecting the eigenstate of this mode onto the phonon eigenstates of undoped $PbTiO_3$ [namely using the phonon states of undoped $PbTiO_3$ as the bases in the right side of Eq.(1.2)]. This reveals which modes at n_e=0 interact in order to form the LFSM at n_e=0.3. The calculated projection coefficients $|p_{ml}|^2$ are depicted in Figure 1.3(a).

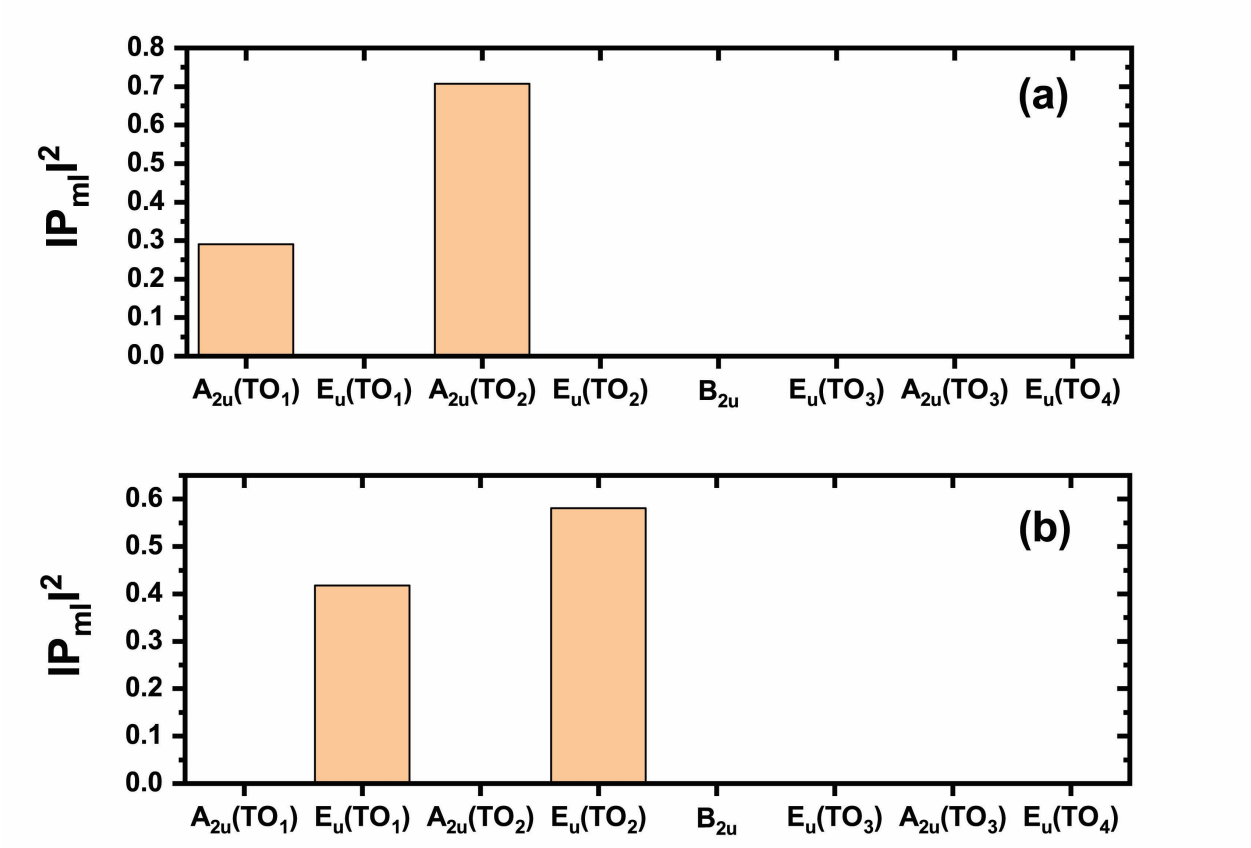

Figure 1.3: Projection magnitude $|p_{ml}|^2$ for: (a) the LFSM at n_e=0.3, (b) the LFSM at n_e=0.6. In both cases, the phonon eigenvectors of undoped $PbTiO_3$ are used as the bases (i.e., the horizontal axis) in the mode projection.

Figure 1.3(a) shows that the LFSM $A_{2u}(TO_1)$ at n_e=0.3 comes from two modes in undoped $PbTiO_3$: 30% from undoped $A_{2u}(TO_1)$ and 70% from undoped $A_{2u}(TO_2)$. Therefore, electron doping causes a mixing of undoped $A_{2u}(TO_1)$ and $A_{2u}(TO_2)$ modes, and it is this mixing that forms the LFSM at n_e=0.3. Furthermore, since the majority contribution to the LFSM at n_e=0.3 comes from the undoped $A_{2u}(TO_2)$ mode, the former must be similar to the latter in terms of eigenstate. This is indeed confirmed by comparing the phonon eigenvector of the LFSM at n_e=0.3 [shown in Figure 1.1(b)] with the eigenvector of undoped $A_{2u}(TO_2)$ [shown in Figure 1.1(d)], where, for both modes, Ti and O atoms move in the same direction while Pb atoms move oppositely. The mode projection thus reveals an interesting finding, namely that the *non-soft* mode $A_{2u}(TO_2)$ in undoped $PbTiO_3$ becomes a soft mode after electrons are doped into the system. Electron doping is thus found to turn a non-soft mode into a soft mode, which is in agreement with the result in Ref.[31].

The mode mixing caused by metallicity is general. For instance, mode mixing is also critical in forming the LFSM at higher n_e=0.6, which vibrates along the inplane direction. In Figure 1.3(b), projection coefficients $|p_{ml}|^2$ of this LFSM are plotted, again using the phonon eigenvectors of undoped $PbTiO_3$ as bases. We see in Figure 1.3(b) that the LFSM at n_e=0.6 originates from the mixing of two undoped modes: 42% from $E_u(TO_1)$ and 58% from $E_u(TO_2)$. The two contributions are nearly 50% each, indicating that the mixing is strong.

The reason that electron doping causes mode mixing can be intuitively understood. It is known that electric field in ferroelectrics generates a strong mode mixing, which leads to the large LO/TO splitting [55, 56]. By introducing additional charges in the system, electron doping alters the long-range Coulomb interaction and behaves like electric field, hence creating the mode mixing. Electron doping also reduces the LO/TO splitting [57].

After having established that electron doping mixes different modes, we now show that the mode-mode interaction is the origin responsible for the unusual persistence of soft modes. (i) First we recognize in Figure 1.2 that, according to the group theory, modes $A_{2u}(TO_1)$

and $A_{2u}(TO_2)$ interact when concentration n_e varies, as witnessed by the fact that these two modes anti-cross near n_e=0.2. The anti-crossing bends downward the $\omega \sim n_e$ curve of $A_{2u}(TO_1)$, and meanwhile lowers the frequency of this mode, which favors the persistence of soft mode to a high doping concentration. If the above anti-crossing had not occurred, the frequency of $A_{2u}(TO_1)$ may have exceeded zero—and polar instability may thus have disappeared—near n_e=0.35. (ii) In Figure 1.2, the slopes of the $\omega \sim n_e$ curves, for $A_{2u}(TO_1)$ at *high* doping concentration $n_e \geq 0.3$ and for $A_{2u}(TO_2)$ [not $A_{2u}(TO_1)$] at *low* concentration $n_e < 0.05$, are interestingly similar and are both flat. This again results from the mode interaction since, according to our projection results in Figure 1.3(a), the LFSM $A_{2u}(TO_1)$ at n_e=0.3 has a large contribution of 70% from $A_{2u}(TO_2)$ at n_e=0. The markedly flat $\omega \sim n_e$ slope for $A_{2u}(TO_1)$ after anti-crossing allows this mode to remain soft at high n_e. Therefore, the anti-crossing between modes is pivotal in the persistence of ferroelectric instability at high n_e.

The fundamental reason behind flat $\omega \sim n_e$ curve is the delicate balance between the following two factors. On the one hand, the electron doping generally *increases* the mode frequency by altering the Coulomb interaction. On the other hand, the electron doping introduces the mode-mode interaction (i.e., the anti-crossing between modes), which *decreases* the frequency of the soft mode by bending downward its $\omega \sim n_e$ curve. The delicate balance of these two factors leads to the possible existence of a flat $\omega \sim n_e$ curve and thus the unusual persistence of soft mode in electron-doped $PbTiO_3$.

Once the importance of the mode-mode interaction is revealed, we now explain why the LFSM transforms from Figure 1.1(a) to Figure 1.1(b) and finally to Figure 1.1(c) as n_e varies. The strong coupling between $A_{2u}(TO_1)$ [i.e., the mode in Figure 1.1(a)] and $A_{2u}(TO_2)$ [i.e., the mode in Figure 1.1(d)], as witnessed by the anti-crossing between them near n_e=0.15 in Fig.1.2, causes these two modes to mix. As a consequence of this mixing, the LFSM at n_e=0.3 (i.e., after anti-crossing) assumes the character of $A_{2u}(TO_2)$, and will resemble the $A_{2u}(TO_2)$ mode at n_e=0, which is indeed confirmed by comparing Figure 1.1(b) with

Figure 1.1(d). This leads to the transformation of the LFSM from Figure 1.1(a) to Figure 1.1(b). In other words, the coupling between the mode in Figure 1.1(a) and the mode in Figure 1.1(d) leads to the LFSM mode in Figure 1.1(b). Transformation from Figure 1.1(b) to Figure 1.1(c) occurs as follows. As shown in Figure 1.2, the slope $\frac{\Delta\omega}{\Delta n_e}$ of the $A_{2u}(TO_1)$ curve is notably larger than the slope of the $E_u(TO_1)$ curve when $n_e < 0.3$. Therefore, when n_e increases, the frequency of $A_{2u}(TO_1)$ rises faster than that of $E_u(TO_1)$. As a result, $E_u(TO_1)$ becomes the lowest-frequency soft mode at n_e=0.6, and thus the LFSM transforms from Figure 1.1(b) to Figure 1.1(c). It is also useful to mention that the distortions in Figure 1.1(b)-(d) are ferroelectric (not anti-ferroelectric), since they all correspond to phonon modes at the zone center q=0. Anti-ferroelectric modes occur instead at the zone boundary.

Our results provide new insight into the persistence of soft modes in electron-doped $PbTiO_3$ polar metal. Previously the persistence of soft modes was attributed to the lone-pair of Pb and the pseudo Jahn-Teller effect which involves only *one* phonon mode[58] (not the mode-mode interaction as we discover in our study). In contrast, we investigate the mode mixing caused by electron doping, and we find that the unusual persistence of soft modes originates from the strong mode-mode interaction which must involve *two* phonon modes. Furthermore, driven by the strong mode-mode interaction mechanism, two more unusual discoveries are made in this study, namely (a) electron doping can turn non-soft mode into soft mode, and (b) the frequency change $\Delta\omega/\Delta n_e$ of soft mode is remarkably flat at high n_e. Meanwhile we should mention that, while we examine the effects of doping on the phonon instability at the zone center, electron doping may also alter the phonon frequencies and change the polar distortion throughout the other part of Brillouin zone [59].

To investigate whether our theory applies to other materials, we have performed calculations for $BaTiO_3$ (which is another important ferroelectric) under different concentrations of electron doping, and the calculation results are given in Figure **??**.

Figure 1.4 shows that (i) soft mode in $BaTiO_3$ disappears at a critical doping concentration n_e^c=0.14, which is much smaller than n_e^c=0.7 in $PbTiO_3$; (ii) the coupling strength

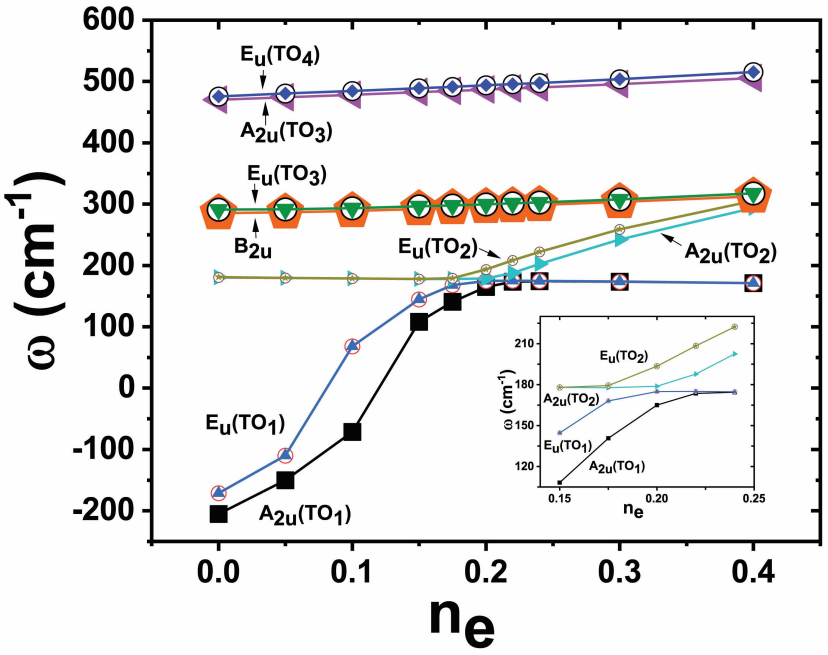

Figure 1.4: Phonon frequencies at Γ point as a function of n_e in electron-doped $BaTiO_3$. Symbols are the results directly obtained from DFPT calculations; lines that depict the mode evolution between different n_e are obtained by mode projection. Labels of normal modes are given near each curve. The inset shows the anti-crossings between $A_{2u}(TO_1)$ and $A_{2u}(TO_2)$ modes near n_e=0.2 and between $E_u(TO_1)$ and $E_u(TO_2)$ near n_e=0.17.

between $A_{2u}(TO_1)$ and $A_{2u}(TO_2)$, as measured by the smallest anti-crossing phonon gap of these two modes, is weak and merely $\sim$14 cm^{-1} for $BaTiO_3$ in Figure 1.4 (see the inset of this figure), as compared to the coupling strength of $\sim$238 cm^{-1} for $PbTiO_3$ in Figure 1.2. The reason that the soft mode disappears at a lower n_e^c in $BaTiO_3$ can be explained by the fact that the weak coupling strength between $A_{2u}(TO_1)$ and $A_{2u}(TO_2)$ in $BaTiO_3$ does not bend the $A_{2u}(TO_1)$ curve downward strongly and does not push the $A_{2u}(TO_1)$ frequency to be below zero in Figure 1.4. The results thus further confirm our main conclusion that the strong mode-mode coupling is the key mechanism which causes the unusual persistence of ferroelectricity in electron-doped $PbTiO_3$.

Mode mixing and mode coupling are equivalent since two modes mix with each other generally when there is an interaction between them. Mode mixing (or mode coupling) is a rather universal phenomena which can occur in many systems such as in the systems with trilinear coupling [18, 20] and in $LaSrMnO_3/LaNiO_3$ superlattice where a hidden phonon mode comes from multi-mode coupling [60]. Our theory can thus be applied to many systems. Meanwhile we find that the coupling need be strong in order for the soft mode to persist at high electron doping as shown in Figure 1.2 for $PbTiO_3$, in contrast with Figure 1.4 for $BaTiO_3$ where coupling is weak.

1.4 Conclusions

In summary, we have studied ferroelectric instability in metallic and doped $PbTiO_3$. We found (i) the instability is remarkably preserved to a high electron concentration of n_e=0.7. (ii) In metallic $PbTiO_3$ under electron doping, the mechanism for generating ferroelectricity is predicted to differ from that in undoped system, and Ti-O opposite motion is no longer a valid mechanism. Instead, ferroelectricity in metallic $PbTiO_3$ is caused by the Pb-O opposite motion. (iii) Intriguingly, electron doping is discovered to turn the non-soft $A_{2u}(TO_2)$ mode into a soft mode. (iv) The slope $\Delta\omega/\Delta n_e$ is revealed to be markedly flat for the soft modes at high n_e, which is critical for the sustaining of FE soft modes under metallic condition.

(v) The strong mode-mode interaction, caused by electron doping, is the origin responsible for the unusual persistence of polar instability in doped $PbTiO_3$. Engineering the mode interaction may extend the limit of metallicity that allows FE. These results yield new knowledge and insight into polar metals and may open future possibility to utilize them for novel applications.

2 Strain-driven metal to polar-metal transition in Nb-doped $PbTiO_3$

2.1 Introduction

2.1.1 Effect of strain on ferroelectrics and polar-metals

Polar metals have dual properties of conductivity and polarity. However, they are rare in nature, because the free electrons screen out the internal dipoles which break the inversion symmetry of the crystal lattice. The first polar metal experimentally discovered by Shi *et al.* is $LiOsO_3$ and it changes from centrosymmetric $R\bar{3}c$ structure to non-centrosymmetric R3c structure at 140 K while keeping its *metallic* state [27]. After this discovery, different theoretical and experimental research groups have been using distinct methods to create a new polar metal. One of such method is doping insulating ferroelectric materials with conducting electrons [31, 32, 58, 61]. Whereas, the other method is a natural selection process without doping where geometric constrains are applied to preserve polar distortion (*decoupling of itinerant electron at the Fermi level from soft transverse optical phonons which causes polar distortion*) [2, 28, 30, 57] and a proposal of short-range interaction mechanism rather than the well know long-range Coulomb interaction to stabilize ferroelectricity (FE) [29].

As we know, the text book definition of ferroelectric is a material owning a spontaneous polarization that can be reversed by the application of an electric field. To claim polar metals as ferroelectric their polarity must be reoriented by applying an electric field. This requirement is yet to be verified experimentally, specially for bulk and superlattice crystalline structure. However, in WTe_2, which is a thin two dimensional layered topological semimetal, the polarity is reversed by an external field [62]. The additional polar character distinguish polar metals from an ordinary metals since it couples with electric, magnetic, and orbital degrees of freedom to provide versatile application in unusual optical response, superconductivity, magnetoelectricity, thermoelectricity, ultra-fast Mott based devices, non-volatile

memories, photovoltaics, and multi-ferroic sensors [20, 24, 58, 63, 64].

In addition to chemical doping, strain has been one of the most important parameter to tune the physical and chemical properties of *perovskite* oxides [65–71]. For example, $SrTiO_3$ does not display a *ferroelectric* structure for any range of temperature, however, when a 1% biaxial tensile strain induced by $DyScO_3$ substrate is applied, it transforms from a *paraelectric* to a *ferroelectric* state at 294 K [72]. $PbTiO_3$ (PTO) is a ferroelectric material that undergoes a single phase transition from cubic to tetragonal structure at T_c=490 K. But, the biaxial compressive strain applied on PTO thin film due to $SrTiO_3$ substrate up on which it is grown significantly change the T_c value to 813 K [73]. Unlike PTO, the ferroelectric instability of $BaTiO_3$ (BTO) is suppressed by doping [31, 32, 74, 75]. However, using X-ray diffraction and second harmonic generation measurement, Takahashi *et al.* observed a low temperature non-polar to polar structural phase transition of La-doped BTO while the doping level of La increased. Moreover, metallicity of the polar phase advances down to 100 K despite the small doping value of La, which is $n = 1.0{\times}10^{14}$ $electrons/m^3$. This result is tied to the compressive biaxial strain applied on La-doped BTO when it is epitaxially grown on $GdScO_3$ substrate [76]. Therefore, strain is also an effective way of tuning the properties of polar metals at a wide range of temperature.

Recently, $PbTi_{1-x}Nb_xO_3$ films fabricated using laser molecular epitaxy technique exhibit a *ferroelectric-like* polar distortion at room temperature. Using piezoresponse force microscopy (PFM), Gu *et al.* observed macroscopic ferroelectric hysteresis loops in these films without any saturated state due to heavy leakage current. As Nb concentration varies from 0.04 to 0.12, the temperature dependent transport properties of these films show a transition from *insulator* to *semiconductor*, and from *semiconductor* to *metallic* state. Furthermore, Nb doping has a very small effect on the dipoles in the unit cell regardless of the doping concentration; its sole effect rather is to provide free electrons [77]. However, in Gu *et al.* computational study *the effect of strain, structural stability, and polar mode* of Nb-doped PTO are not investigated in detail to complement the experimental probe. Hence, more

computational studies are necessary to better understand the *polar metal* characteristics of Nb-doped PTO on the fundamental level. In particular, since structural stability of PTO is governed by its phonon frequencies at the Γ point, it is realistic to analyze the phonon frequencies and polar mode of Nb-doped PTO. Therefore, this paper will give emphasis on those topics and examine the effect of biaxial compressive strain (η) on the *polar mode* of Nb-doped PTO.

In this study, employing density functional theory (DFT) and density functional perturbation theory (DFPT), we studied how the polar mode ($A_{2u}(TO_1)$) of Nb-doped PTO at the Γ point can be tuned under different biaxial compressive strain. Our study shows that $A_{2u}(TO_1)$ became stable when -2% and -3% biaxial strains are applied on Nb-doped PTO, i.e., its energy changes dramatically from -0.095 meV to -29.51 and -39.56 meV, respectively. As a result, Nb-doped PTO could be used as a room temperature polar metal. We also found out that the wave function of the additional electron achieved when Ti is replaced by Nb is *localized and form small polarons* state since the electron density (n) is 2.16×10^{21} cm^{-3}, which is one order of magnitude greater than 10^{20} cm^{-3} [78]. This state can be thermally triggered into a conductive state. Moreover, the slope of the average potential graph indicates that the extra electron partially screens out the electric field existed in the pure $PbTiO_3$ (i.e., without Nb doping).

2.2 Methods

We combined eight bulk cubic (a=3.88 Å) PTO to create a 1×1×8 supercell (SC) of 40 atoms (a=3.88 Å and c/a=8), and then one tetravalent Ti atom is substituted by pentavalent Nb atom to make the system *metallic*. Because, TiO_2 has zero net charge, whereas NbO_2 has a net charge of -e. Therefore, Nb-doped PTO has one extra electron. Due to the comparable atomic radius of Ti (r=0.64 Å) and Nb (r=0.61 Å), the lattice mismatch introduced by this substitution is very small [79]. We choose to work on Nb-doped PTO since it can be experimentally synthesized employing epitaxy techniques [77].

2.2.1 Density functional theory (DFT)

We use Density functional theory (DFT) within the local-density approximation [34, 35] as implemented in the plane wave pseudopotential code of Quantum Espresso [36, 37] to compute total energy, atomic force, and optimal structure. The energy cutoff for the plane-wave expansion of single-particle states is 100 Ry and 6×6×2 Monkhorst-Pack k-mesh is used to sample the Brillion zone. Norm-conserving pseudopotentials are used [38]. Semicore $3s$ and $3p$ states of Ti are treated as valence states to ensure better accuracy [39, 40].

2.2.2 Density functional perturbation theory (DFPT)

We relaxed the atomic structure while keeping *centrosymmetry* to ensure the existence of ferroelectric instability; the phonon frequencies and eigenvectors are computed using the linear-response density functional perturbation theory (DFPT) [41–43]. When atoms vibrate, the shifts of atoms induce a deformation potential $\Delta V(\mathbf{r})$ of bare ions, which is treated as perturbation. The linear response of electron state $\Delta\psi_n(\mathbf{r})$ is computed [41, 42] by solving the Sternheimer equation:

$$(H_{scf} - \varepsilon_n)|\Delta\psi_n\rangle = -(\Delta V_{scf} - \Delta\varepsilon_n)|\psi_n\rangle \tag{2.1}$$

where H_{scf} is the Kohn-Sham Hamiltonian, ε_n the eigenvalue of H_{scf}, $\Delta V_{scf}(\mathbf{r}) = \Delta V(\mathbf{r}) + e\int \frac{\Delta n(\mathbf{r\prime})}{|\mathbf{r}-\mathbf{r\prime}|}\,\mathrm{d}\mathbf{r\prime} + \frac{dv_{xc}(n)}{dn}\Big|_{n=n(\mathbf{r})} \Delta n(\mathbf{r})$ the first-order correction to the $V_{scf}(\mathbf{r})$ potential, and $\Delta\varepsilon_n$=$\langle\psi_n|\Delta V_{scf}(\mathbf{r})|\psi_n\rangle$ is the first-order correction to eigenvalue ε_n. The variation of electron state $\Delta\psi_n(\mathbf{r})$ is computed by solving the Sternheimer equation [44].

The minimum energy (E_{min}) of $A_{2u}(TO_1)$ without any strain is -0.095 meV, which is not stable under ambient temperature (K_BT∼25 meV). Hence, -1%, -2%, and -3% biaxial strain are applied to alter this energy. Note that, tensile strain will eliminate E_{min} and that is why we used compressive strain instead of tensile strain. Then, we relaxed the supercell structure to find optimal atomic positions and c/a values for each η.

Table 2.1: Crystal structure Nb-doped PTO and its soft mode ($A_{2u}(TO_1)$) frequencies under different η. The imaginary frequencies of the soft mode are given as negative freqencies.

η (%)	a (Å)	c/a	c (Å)	Unit cell volume (Å ^{3})	ω (cm^{-1}) of $A_{2u}(TO_1)$	E_{min} of $A_{2u}(TO_1)$ in meV
0	3.88	8.0000	31.04	467.29	-13.82	-0.095
-1	3.84	8.2245	31.58	465.67	-56.31	- 18.26
-2	3.80	8.4080	31.95	461.36	-70.86	-29.51
-3	3.76	8.5869	32.29	456.50	-78.81	-39.56

2.3 Results and Discussions

2.3.1 Crystal structure of Nb-doped PTO

A 1×1×8 supercell consists of 40 atoms is constructed by combining eight bulk cubic *centrosymmetric* PTO, which has a lattice constant of $a = 3.88$ Å. Then, Ti is replaced by Nb to make the SC *metallic*, and we relaxed this structure with fixed in-plane lattice constant $a = 3.88$ Å and tetragonality $c/a = 8.00$ while keeping centrosymmetry; otherwise, ferroelectric instability is not guaranteed. The minimum energy of the *polar mode* for this particular structure is -0.095 meV, which is unstable under room temperature condition. Hence, we applied strain to tune the minimum energy of this mode; detail analysis about the *ploar mode* is given later.

Similarly, by fixing the in-plane lattice constant a after applying -1%, -2%, and -3% strain to Nb-doped PTO, the SC structure is relaxed to find the optimal values of c and final atomic positions for each strain. The optimal value of c is given on the fourth column of Table 2.1. When the in-plane lattice constant a shrinks due to the biaxial compressive strain, the tetragonality c/a elongates. Furthermore, the unit cell volume decreases while η increases as shown on the fifth column of Table 2.1.

2.3.2 Partial and total phonon density of states (DOS) of pure and Nb-doped PTO

After calculating the phonon frequencies employing DFPT, we further analyze the partial and total phonon DOS for pure and Nb-doped PTO to understand individual phonon frequency contribution from each atom, and how the substitution of Ti by Nb affect the *polar mode*. The

word *polar mode* and *soft mode* are used interchangeably throughout this project. Phonon frequencies are computed using the optimized lattice vectors of -2% biaxially strained Nb-doped PTO, i.e., the in-plane lattice constant a and tetragonality c/a are 3.80 Å and 8.4080, respectively. The partial and total phonon DOS of pure and Nb-doped PTO are illustrated in Figure 2.1. We have applied acoustic sum rule (ASR) for all phonon frequencies to exclude the trivial three acoustic modes with zero frequency (due to translational invariance of space) and to account for the long range nature of interatomic force constants due to the dipole-dipole interaction at the Γ point. Hence, these modes are not included in Figure 2.1 and Figure 2.2. The total DOS is given by

$$D(\omega) = \sum_{s,q} \delta(\omega - \omega_{s,q}) = \sum_{s} D_s(\omega) \ , \tag{2.2}$$

where s, q, and $D_s(\omega)$ are phonon modes, phonon wavevector, and partial DOS, respectively. Each mode s can contribute $D_s(\omega)$ to the total DOS $D(\omega)$.

It is inferred from Figure 2.1(a) and (b) that the phonon modes extend up to 706.64 and 688.38 cm^{-1} for pure and Nb-doped PTO, respectively. When Ti is substituted by Nb, the number of *soft mode* decreased from two to one, and the frequency of this mode became less negative due to the screening effect of the additional electron on the long-range Coulomb interaction. The *soft mode* frequencies of pure PTO are -102.35 and -70.44 cm^{-1}, whereas the *soft mode* frequency of Nb-doped PTO is -70.86 cm^{-1}. Therefore, the effect of Nb doping is just to partially screens out the internal dipoles, and the *ferroelectric instability* is preserved in Nb-doped PTO. In fact, in our previous study, we have showed that the *ferroelectric instability* of bulk PTO (5 atoms per unit cell) can be sustained up to an electron concentration of n_e=0.7 per unit cell [75]. Furthermore, this substitution does not significantly affect ω as shown in from Figure 2.1(b): the shift of ω from left to right for the *soft modes* and from right to left for *non-soft modes* phonon is about less than 40 and 20 cm^{-1}, respectively.

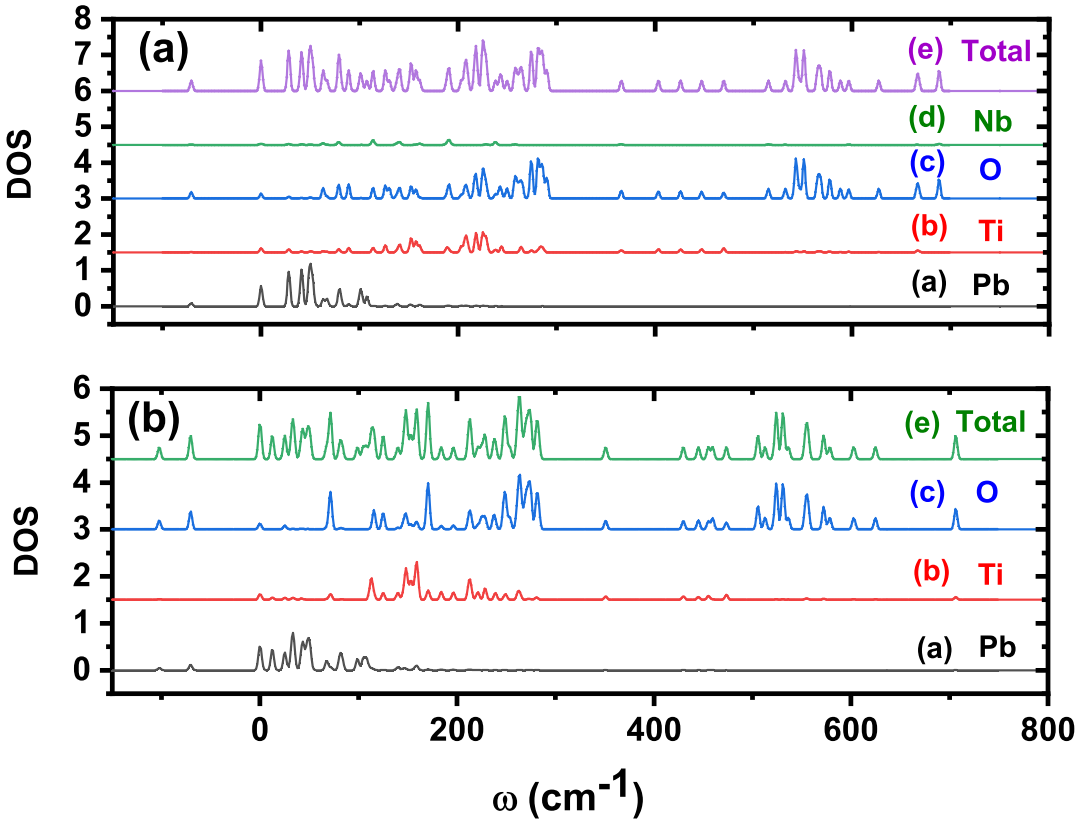

Figure 2.1: Partial and total phonon density of states of (a) Nb-doped PTO and (b) pure PTO at the Γ point. The contributions from each atom to the total DOS is designated with atomic symbols at the right hand side of this figure for both pure and Nd-doped PTO. The same range of frequencies on the x-axis are used for the sake of convenience and comparison, and 2% biaxial compressive strain is applied for both pure and Nb-doped PTO.

The *soft mode* frequency is predominantly due to Pb and O as shown in Figure 2.1. Even if Ti contribution to the soft mode is not clearly seen on Fig. 2.1 due to the scale used for DOS, it has a very small involvement which can not be neglected as depicted in Figure 2.3(a). Hence, the *ferroelectric instability* of Nb-doped PTO is caused by antiparallel displacement of both Pb-O and Ti-O atoms unlike the electron doped bulk PTO, where only the opposite displacement of Pb and O drives the *ferroelectric instability* [75].

The total DOS illustrates that the phonon modes ω of pure and Nb-doped PTO conglomerate approximately into three groups (excluding the soft modes) with frequencies 0-110, 110-300, and > 300 cm^{-1}. As a result, the frequency bands are divided more or less into three bands in both cases: high, medium, and low frequency bands. O, Ti-O, and Pb-O are participated in high, medium, and low range of ω, respectively for both pure and Nb-doped PTO as can be seen from the partial DOS in Figure 2.1. This is because of the difference in atomic masses of the constitute elements and the electro static Coulomb interaction of Pb-O and Ti-O .

2.3.3 Phonon mode average distance from Nb and localized phonon modes

Denote the zone-center phonon eigenvector as $|\epsilon_{i\alpha}\rangle$, where i is the atom index and α is the direction index. Eigenvector $|\epsilon_m^{i\alpha}\rangle$ is related to the phonon displacement $|u_m^{i\alpha}\rangle$ by $|\epsilon_m^{i\alpha}\rangle = \sqrt{M_i}|u_m^{i\alpha}\rangle$, where M_i is the mass of atom i. To locate each phonon mode's position from Nb, we have calculated the phonon mode average distance from Nb along the z direction in Å as

$$r_\alpha = \sum_i W_i \left|\vec{r}_{i\alpha} - \vec{r}_{Nb,\alpha}\right| , \tag{2.3}$$

where W_i=$\sum_\alpha |\epsilon_{i\alpha}|^2$. The phonon mode average distance from Nb is shown in Figure 2.2. There are two localized phonon modes (mode 36 and 119) as indicated in Figure 2.2. Localized phonon modes are defined as phonon modes which are located very close to Nb site. Mode 36 and 119 are at a distance of 0.07 and 0.04 Å from Nb, respectively.

Furthermore, most phonon modes are within 7-11 Å from Nb, and these are predomi-

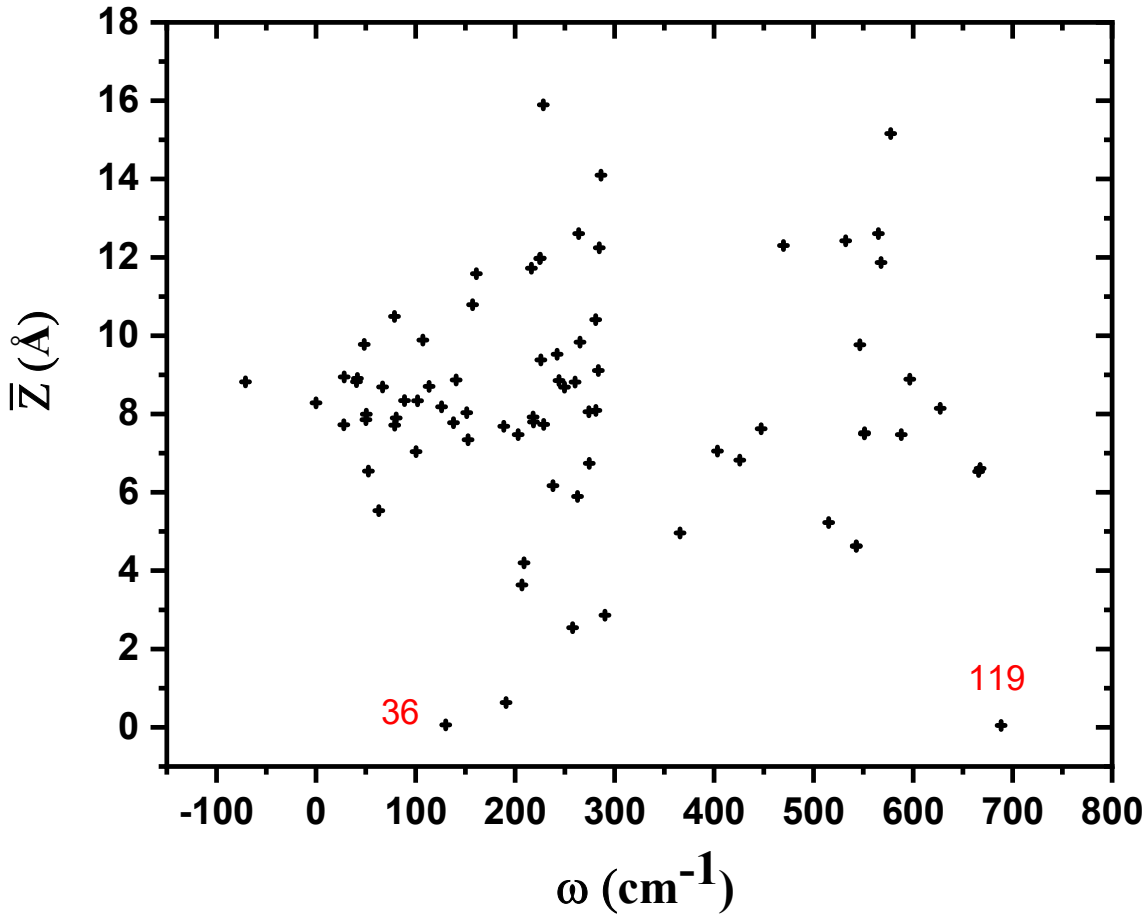

Figure 2.2: Mode average distance from Nb in the Z direction of -2% strained Nb-doped PTO. Localized phonon modes are identified with their mode numbers. Most phonon modes are within 7-10 Å from Nb, and it is apparent that the frequency of most phonon modes are less than 300 cm^{-1}.

nantly low and medium frequency modes ($\omega < 300 cm^{-1}$); which is in agreement with Figure 2.1. Mode localization is associated with the application of biaxial compressive strain, because *unstrained* (η=0%) Nb-doped and pure PTO have similar $\bar{Z}$ vs ω graph. The existence of most phonon modes within 7-11 Å from Nb is mainly associated with the breaking of translational symmetry by the impurity atom Nb, in addition to biaxial compressive strain, and thereby alter the interatomic interactions, which in turn governs the lattice dynamics.

2.3.4 Soft, localized, and impurity phonon modes

The phonon eigenvector of $A_{2u}(TO_1)$ is depicted in Figure 2.3(a), and the dynamical polarization is due to the opposite displacement of Pb-O and Ti-O atoms. However, Pb-O displacement is larger than Ti-O; in particular, Pb atomic displacement is larger than Ti. This result is in agreement with the DOS analysis; Pb participates at low ω range since its atomic mass is the heaviest of the rest of the atoms, and the frequency of $A_{2u}(TO_1)$ is -70.86 cm^{-1}.

localized phonon mode 36 is shown in Figure 2.3(a). Impurity phonon mode is defined as a phonon mode with heavy participation of impurity Nb, and this can be distinguished by large displacement of Nb in the phonon eigenvectors. Indeed, the phonon eigenvector of impurity phonon modes support the presence of such displacement. Metals like Pb and Nb have strong electron-phonon interaction [80]; since the extra electron in Nb-doped PTO is localized at Nb site, the presence of impurity phonon modes might facilitate the electron-phonon coupling mechanism of superconductivity in this system.

Localized phonon modes have one large peak at Nb-O_2 plane, and the analysis of their phonon eigenvectors confirms that all of them have one common feature, i.e., their eigenvectors are preponderantly due to either the in-plane or out of plane opposite displacement of oxygen atoms that are on the plane of Nb-O_2. When O atoms that are on the edge of octahedral moving antiparallel in the Z-axis, Nb displacement is entirely zero. Because, it can not move along this axis without interacting with nearby O and Ti atoms, which cost

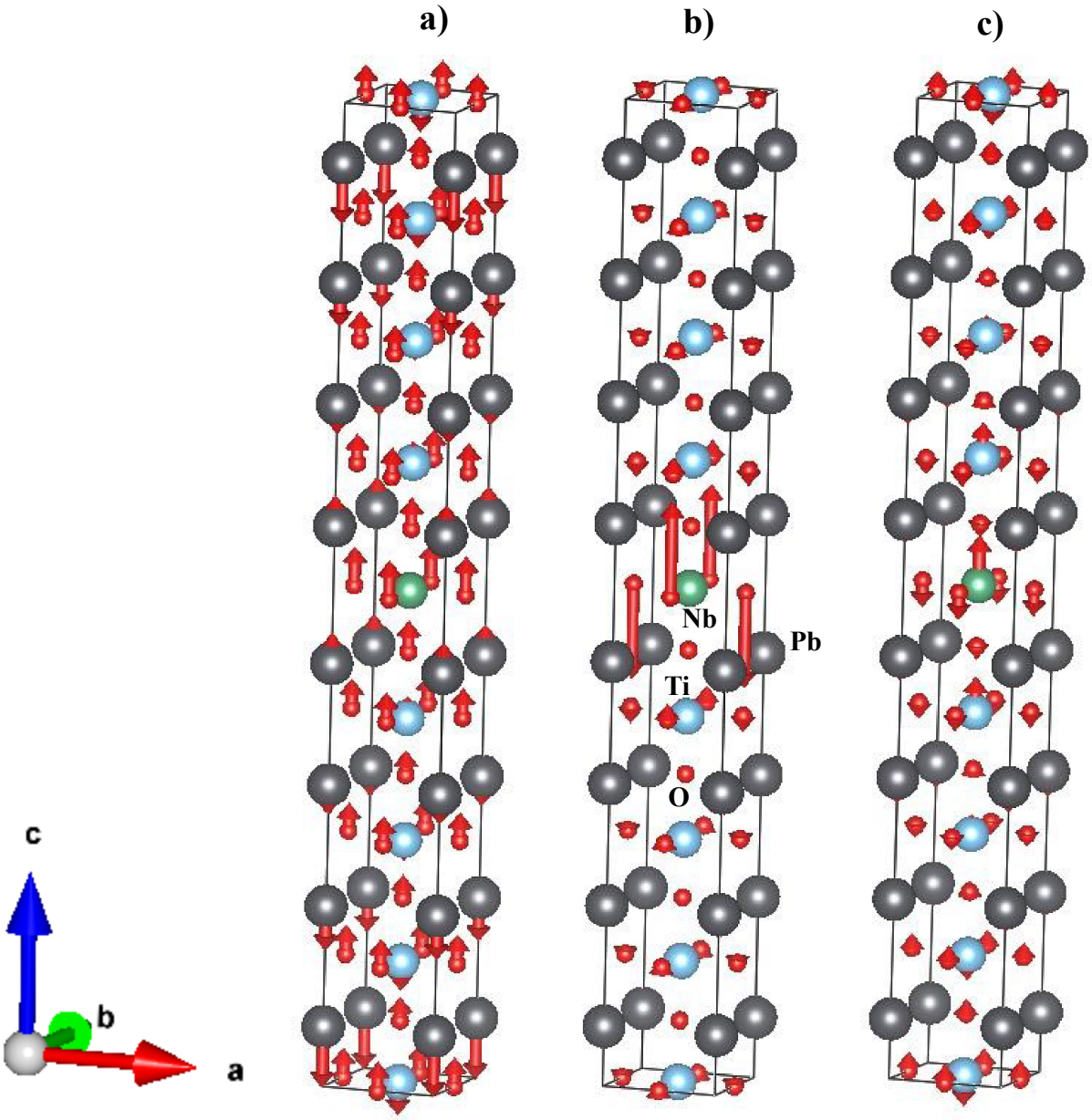

Figure 2.3: Phonon eigenvector of -2% strained Nb-doped PTO: (a) soft mode (b) localized mode, and (c) impurity mode. Arrow and its length indicate the vibration direction and amplitude, respectively.

more energy than the in-plane antiparallel displacement of O atoms, where Nb has small displacement due to the electrostatic attractive Coulomb interaction between O and Nb ions. However, the displacement of O is more than 50% to that of Nb.

2.3.5 Average potential ($\bar{V}$) and $\Delta\rho$ in one and two dimensions

The extra electron provided by the Nb doping does alter the frequency of the *soft mode*; the frequency of this mode becomes less negative when Nb is replaced by Ti. This electron also changes ($\bar{V}$) as shown in Figure 2.4(a). From Coulomb electrostatic equation we know that the electric field (E) is given by $E = -\nabla\bar{V}$. Hence, Fig. 2.4(a) illustrates that there is a clear distinction between the slope of $\bar{V}$ for pure and Nb-doped PTO: the slope of $\bar{V}$ of the former one is larger than the latter one. As a result, E of Nb-doped PTO is smaller than E of pure PTO. The difference in the trend of $\bar{V}$ is due to the screening effect of the extra electron on the long range Coulomb interaction. The slope of $\bar{V}$ is shown on Figure 2.4(a) with red and black dashed lines for pure and Nb-doped PTO, respectively. Nb-doping has also an effect on the charge density, and it will be discussed below.

To understand whether the free carrier is localized or delocalized, its effect on the charge density of Ti, and how this varies on the x-z plane; we have computed the difference in charge density as $\Delta\rho(\mathrm{Z}) = [\rho_d(\mathrm{Z}) - \rho_p(\mathrm{Z})]$ in 1D and $\Delta\rho(\mathrm{X,\ Z}) = [\rho_d(\mathrm{X,\ Z}) - \rho_p(\mathrm{X,\ Z})]$ in 2D. Where, d and p stand for Nb-doped and pure PTO, respectively. Then, we have plotted the line and contour charge density (n) for 1D and 2D, respectively. The 1D charge density is achieved by integrating the 3D charge density over dx and dy, whereas the 2D charge density is achieved by integrating the 3D charge density over dy.

For the 1D charge density, Figure 2.4(b) illustrated that the wavefunction of the charge density is localized in the vicinity of Nb and dies out abruptly away from it. Moreover, n is negative at the site of Nb, which implies the presence of excess electron. However, n is positive at the site of O (the two peaks with positive value of $\Delta\rho$), which implies the deficiency of electron. The charge density n of -2% strained Nb-doped PTO is 2.16×10^{21}

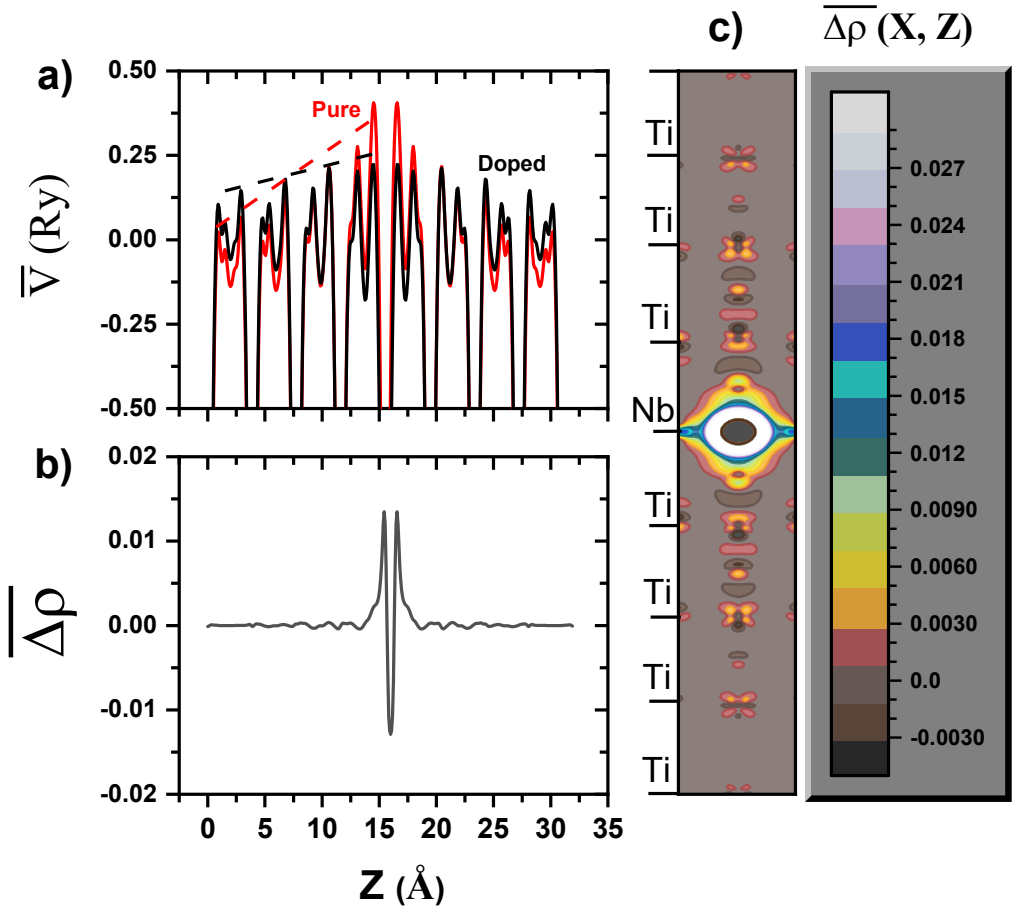

Figure 2.4: (a) Average potential ($\bar{V}$) of -2% strained PTO. The red and black colors with solid lines are used for $\bar{V}$ of pure and Nb-doped PTO, respectively. The slopes of $\bar{V}$ for pure and Nb-doped PTO are schematically drawn with red and black dashed lines, respectively. (b) The difference in charge density: $\Delta\rho(\mathrm{Z}) = [\rho_d(\mathrm{Z}) - \rho_p(\mathrm{Z})$ of -2% biaxially strained PTO. Subscript d and p stand for Nb-doped and pure PTO, respectively. The wavefunction of $\Delta\rho$ is localized in the vicinity of Nb. (c) The difference in charge density: $\Delta\rho(\mathrm{X}, \mathrm{Z}) = \rho_d(\mathrm{X}, \mathrm{Z})$ $- \rho_p(\mathrm{X}, \mathrm{Z})$ of -2% biaxially strained PTO. Subscript d and p stand for Nb-doped and pure PTO, respectively. Nb and Ti sites are labelled with their symbol. To access the values of $\Delta\rho$ at all Ti sites, its range is restricted in between 0.03 and -0.002. The $3d_{xz}$ orbital of Ti atom has asymmetric charge distribution, and the value of $\Delta\rho$ is given on the righthand side of this figure.

cm^{-3}, and according to Ref. [78], if n of a system is greater than 10^{20} cm^{-3}, the electrons will be localized and form small polarons; these electrons could be thermally triggered into a conductive state. However, if n less than 10^{20} cm^{-3}, the electrons will be delocalized and form large polarons. Indeed, our result is in agreement with this study: the extra electron in Nb-doped PTO is localized near Nb.

For the 2D charge density, Figure 2.4(c) depicted that the $3d_{xz}$ orbitals of Ti atom has asymmetric charge distribution, in particular those two $3d_{xz}$ orbitals below and above Nb. This asymmetricity is not only due to the electrostatic Coulomb interaction of the 5s orbital of Nb atom with the $3d_{xz}$ orbital of Ti atom but also due to the application of biaxial compressive strain on Nb-doped PTO. Because, even if we are not included the figure here, the 2D charge density of *unstrained* Nb-doped PTO reveal less charge asymmetricity of Ti $3d_{xz}$ orbitals. Away from Nb, charge asymmetricity decreases since the strength of Coulomb interaction decreases as the distance between charges increases.

The magnitude of charge at the site Nb is larger than to that of Ti sites. For example, the white shaded area at Nb site represent a magnitude of charge larger than 0.03. Note that, the range of $\Delta\rho$ is restricted in between 0.03 and -0.002 to see the charge density on all Ti sites as clearly as possible. But, if a range of $-0.656 \leq \Delta\rho \leq 0.1060$ is used, the white shaded area is exactly 0.106 and large negative value of $\Delta\rho$ at the site of Nb with values -0.5 and -0.6 to list some can be shown. Hence, the localization of electron is further supported by the existence of more negative charge at the site of Nb. The charge density on Ti site corresponding to yellow shaded area is about 0.008.

2.3.6 Double well potential depth (E vs λ) of $A_{2u}(TO_1)$

Potential well of a prototype ferroelectric material in harmonic approximation, which undergoes a second-order phase transition when $T < T_0$ ($T_0 \sim T_c$) has two equivalent minimum energies corresponding to opposite polarization that can be reversed by an application of external field [6, 81]. The potential well depth of *unstrained* Nb-doped PTO is -0.095 meV,

which is unstable under room temperature condition. Because, $K_BT \sim 25$ meV is much greater than 0.095 meV, and thus the unstrained Nb-doped PTO will not show *polar* character when the temperature is elevated to 300 K. Therefore, we have applied -1%, -2%, and -3% biaxial strain on Nb-doped PTO to tune the depth of the potential well energy.

New atomic positions $|r\rangle$ is used to find the total energy E, by scaling the old atomic position $|r_0\rangle$ with a parameter λ as

$$|r\rangle = |r_0\rangle + \lambda|u\rangle \ , \tag{2.4}$$

where $|u\rangle$ is the eigendisplacement of $A_{2u}(TO_1)$, and λ is varied in an interval of 0.02. Note that, $A_{2u}(TO_1)$ is a *soft mode* as shown on the sixth column of Table 2.1.

E vs λ of $A_{2u}(TO_1)$ at three different η is shown in Figure 2.5. The double well potential depth of -1% biaxially strained Nb-doped PTO has E_{min} of -18.26 meV. Hence, an energy gain of 18.17 meV is achieved by applying -1% biaxial strain on Nb-doped PTO; which is a remarkable energy gain given E_{min} of *unstrained* Nb-doped PTO is -0.095 meV. Moreover, there is an energy gain of about 10 meV when η is increasing from -1% to -2%, and from -2% to -3%. By comparing E_{min} with 25 meV, -2% and -3% biaxially strained Nb-doped PTO could be considered as a room temperature polar metal. Since, the energy of those two systems are greater than 25 meV, and the *polar* character would be preserved at room temperature. To change the direction of polarization, an energy greater than 29.51 and 39.56 meV should be supplied to overcome the energy barrier of -2% and -3% biaxially strained Nb-doped PTO, respectively.

The *polar instability* of $A_{2u}(TO_1)$ is increasing while η is increasing: E_{min} of the double well potential becomes more negative when this strain is increasing. Furthermore, the frequencies of $A_{2u}(TO_1)$ mode, which is given in the sixth column of Table 2.1 becomes more negative when the value of η is increasing; this confirms the enhancement of *polar instability* in Nb-doped PTO as η increases. Therefore, a transitions from *metal* to *polar metal* in Nb-

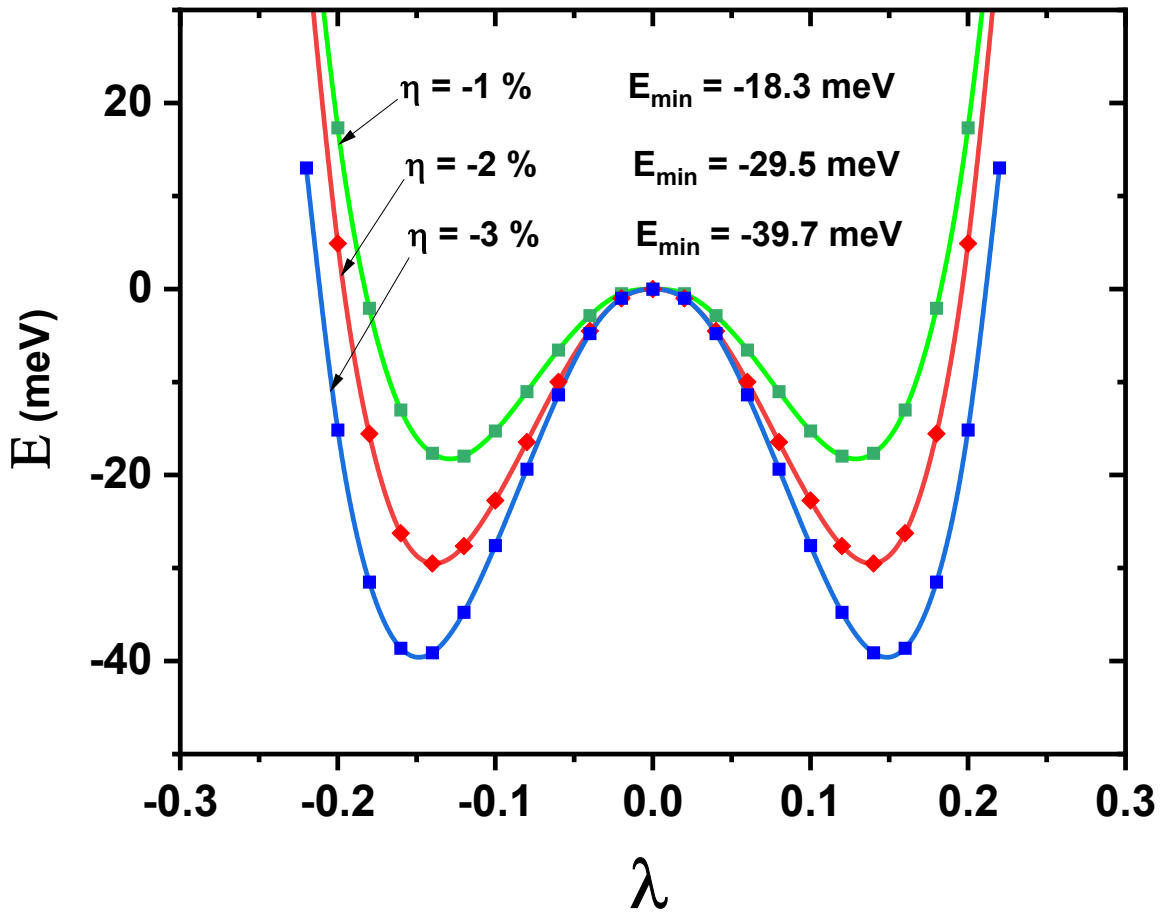

Figure 2.5: $A_{2u}(TO_1)$ double well potential depth of Nb-doped PTO at different biaxial compressive strain (η). Green, red, and blue colors are used for the double well potential at η=-1%, -2%, and -3%, respectively. The value of minimum energies (E_{min}) are indicated for each biaxial compressive strain.

doped PTO is achieved by applying biaxial compressive strain, which tune E_{min} of $A_{2u}(TO_1)$ mode to a desirable value.

2.4 Conclusions

In conclusion, we have studied *polar metal* properties of Nb-doped PTO under -1%, -2%, and -3% biaxial strain. The dopant Nb solely provides a free carrier to make the system *metallic*. We found (i) the biaxial compressive strain enhance the localization of phonon modes, and the eigenvector of these modes are predominantly due to the opposite displacement of oxygen atoms. (ii) ω of most phonon modes of -2% biaxially strained Nb-doped $PbTiO_3$ are less than 300 cm^{-1}. (iii) The unit cell volume decreases when η increases, and ω of $A_{2u}(TO_1)$ becomes more negative as η increases. (iv) The wavefunction of the free carrier is localized in the vicinity of Nb and form a small polaron state, which can be thermally excited into a conduction states. (v) The asymmetry of the $3d_{xz}$ orbitals of Ti atom reveal the existence of *polar* character in Nb-doped PTO (vi) Remarkably, the *metal to polar metal transition* in Nb-doped PTO is driven by the application of biaxial compressive strain since the *unstrained* Nb-doped PTO shows unstable potential well; -2% and -3% biaxially strained Nb-doped PTO can be considered as a room temperature polar metal, because the potential well is stable, and their E_{min} is greater than 25 meV. Therefore, engineering perovskite oxides with both dopant and strain would give a material with new physical and chemical properties, which can have versatile application in science and technology. It is our hope that this study render new insight about the discovery of room temperature *polar metal*.

3 Tuning Rashba interaction and electron-phonon coupling in BiTeI by charge doping

3.1 Introduction

Interaction of electron spin with its orbital angular momentum is crucial in spin-polarized field effect transistor and spin Hall effect, and it is a dominant contribution to the spin-splitting of bands in a narrow band semiconductors [82]. BiTeI is one of such system with a band gap of 1.2 eV, which shrinks to 0.3 eV when spin-orbit interaction (SOI) is included [83]. Moreover, BiTeI is a non-centrosymmetric semiconductor. The spin-splitting of bands in systems that lack an inversion symmetry due to strong SOI leads to many novel physical phenomena such as the spin Hall effect [84], the Edelstein effect [85], magnetoelectric effect [86], the spin Galvanic effect and non-centrosymmetric superconductivity [87–91]. In a conventional superconductors (Pb, Al, Nb, and Nb_3Sn,), the crystal has an inversion symmetry, and this leads to the classification of superconductors by the parity of the pair state as spin-singlet (even parity) and spin-triplet (odd parity) under the sign change of momentum. In unconventional superconductors (UBe_13, UPt_3, MnSi, and $CePt_3Si$) however, the crystal lacks an inversion symmetry. As a result, the above classification is no longer valid when the SO interaction is strong enough to mix the two states [92–97]. Spin Hall effect is observed experimentally using Kerr rotation microscopy in GaAs and InGaAs even though the magnitude of spin polarization was small [82]. For two band Rashba Hamiltonian, the SO interaction can be written as,

$$H_R = \alpha_R \overrightarrow{\sigma} \cdot \overrightarrow{k} \times \overrightarrow{e}_3 \ , \tag{3.1}$$

where α_R is the Rashba parameter, $\overrightarrow{\sigma}$ are the Pauli matrices, and $\overrightarrow{k}$ is crystal momentum [83, 98].

Electron-phonon interaction (EPI) plays an indispensable role in condensed matter physics,

and is observable in many phenomena, such as phonon-assisted optical transition [99], electron mobility in monolayer and bilayer MoS_2 [100], high-temperature superconductivity in compresses H_3S [101], temperature dependent photoluminescence in hybrid perovskites [102], electron mass enhancement in MgB_2 [103], electrical resistivity and superconductivity [104], Khon effect [105], and Peierl's instability [106, 107]. Unlike intrinsic semiconductors and insulators, EPI is well defined for metals, and its strength can be quantified by the electron-phonon coupling constant (λ). λ is a dimensionless quantity, and its typical value ranges in between 0 and 2. Larger λ corresponding to stronger EPI. Thus the study of EPI in doped BiTeI is crucial to look for possible superconductivity.

Chemical and charge doping are used to manipulate the physical and chemical properties of a material. For example, doping $SrTiO_3$ with small amount of Nb changes it from insulator to a conductor, ferromagnetic, and even superconductor [78, 108]. Introducing electrons or holes by charge doping also changes ferroelectrics to polar-metals [31, 32, 75]. The spin precession angle in a field effect spin transistor is proportional to α_R=2E_R/K_F, which is controlled by a gate voltage (V_g) in InGaAs/InAlAs quantum well [82]. Furthermore, as V_g becomes more negative, α_R increased and vice versa; because, the increase of negative V_g leads to the decrease of carrier concentration (electrons) and pushes down the Fermi wave number, k_F. Therefore, in this paper, we investigate thoroughly how the Rashba energy (E_R), Rashba momentum (K_R), Rashba parameter (α_R), and λ of BiTeI can be tuned when different electron and hole concentrations (n_e) are introduced to the system. We showed that E_R, K_R, and α_R varied in a wide range of doping level. In general, hole doping is larger than electron doping for the aforementioned physical quantities. Hence, it is fair to say that BiTeI could be a potential candidate for hole-based spintronics device and p-n junction transistors. λ shows different behavior for electron and hole doping. The former one has a minima, whereas the later one increase monotonically with hole concentration. For E_F = 4.5 eV, the value of λ and the critical temperature (T_C) are found to be 0.44 and 0.7 K, respectively. T_C is somehow small compared with other systems, however, λ of BiTeI is

comparable to Al and Mo [109].

3.2 Methods

We use Density functional theory (DFT) within the local-density approximation [34, 35] as implemented in the plane wave pseudopotential code of Quantum Espresso (QE) [36, 37] to compute total energy, atomic force, and optimal structure. The energy cutoff for the plane-wave expansion of single-particle states is 40 Ry and 6×6×4 Monkhorst-Pack k-mesh is used to sample the Brillion zone. BiTeI is a polar semiconductor, and it has a trigonal symmetry with a space group of p3m1 in which Bi, Te, and I are stacking along c axis alternatively. Our structural optimization yields an inplane lattice constant a=4.27 Å and out of plane lattice constant c=6.63 Å. These values are in good agreement with not only previous theoretical result of a=4.31 Å and c=6.64 [98] but also with experimental result of a=4.34 Å and c=6.85 [110].

For the band structure calculation, we have employed 12×12×8 Monkhorst-Pack k-mesh to obtain the charge density. This choice of k-mesh is used to offset the small degauss (σ) value of 0.006 Ry. $\sigma = 0.006$ Ry provides the correct band structure with respect to electron and hole doping. For example, without doping, the E_F lies in between the conduction band minimum (CBM) and the valance band maximum (VBM), which is the correct position of E_F since BiTeI is a semiconductor material. Other choice of σ provide inconsistent results: i.e., E_F is either above or below CBM and VBM, respectively. In this case, BiTeI is no longer a semiconductor material.

For the EPI calculation, we have resorted to Electron-phonon Wannier (EPW) [111, 112] module that is integrated with QE package, because this package alone can't handle EPI computation with SOI and magnetization simultaneously. EPW make use of Density Functional Perturbation Theory and Maximally Localized Wannier Functions (MLWF) to compute different properties of EPI. This interaction requires a very dense K and q mesh points to accurately describe its matrix element, and MLWF decreases the computational

cost to do so by converting Bloch state to Wannier using Fourier interpolation. Because, Wannier functions (w_{nR}) are spatially localized functions centered on a lattice vector R, whereas Bloch states are extended states all over the lattice.

$$w_{nR}(\mathbf{r}) = \frac{V}{(2\pi)^3} \int_{BZ} \left[\sum_m U^k_{mn} \psi_{mk}(\mathbf{r}) \right] e^{-ik\cdot R} dk \tag{3.2}$$

The EPI matrix elements are give by

$$g^v_{mn}(\mathbf{k},\, \mathbf{q}) = < \psi_{m\mathbf{k}+\mathbf{q}} | \partial_{\mathbf{q}v} | \psi_{mk} >, \tag{3.3}$$

where $\psi_{m\mathbf{k}}$ is the electronic wavefunction for band m and wavevector $\mathbf{k}$. $\partial_{\mathbf{q}v}$ is the derivative of the Kohn-Sham self-consistent potential associated with a phonon wavevector $\mathbf{q}$, branch index v, and frequency ω_{qv} .

Mode resolved electron-phonon coupling constant ($\lambda_{\mathbf{q}v}$) is give by

$$\lambda_{\mathbf{q}v} = \frac{1}{N_F w_{qv}} \sum_m w_k |g^v_{mn}(\mathbf{k},\, \mathbf{q})|^2 \delta(\epsilon_{nk}) \delta(\epsilon_{mk+q}) \tag{3.4}$$

where w_k is the weight of the $\mathbf{k}$ points. The total λ is computed by adding together $\lambda_{\mathbf{q}v}$ over the phonon wavevector $\mathbf{q}$ and branch v as

$$\lambda = \sum_{\mathbf{q}v} w_q \lambda_{\mathbf{q}v} \tag{3.5}$$

where w_q are the weights of the phonon wavevectors $\mathbf{q}$.

After testing the convergence criteria of λ for different values of nkf and nqf, we have selected $nkf = 60{\times}60{\times}48$ the fine electron grids and $nqf = 16{\times}16{\times}12$ for the fine phonon grids. These fine grids are used to compute the superconductivity characteristics of BiTeI. Supplemental information about convergence criteria are given on the Appendix.

3.3 Results and Discussions

3.3.1 Electronic structure of BiTeI

We have calculated the electronic band structure of BiTeI for electron doping of n_e=-0.0125, -0.025, -0.05, and -0.1. For hole doping, we have used the same concentration of n_e=0.0125, 0.025, 0.05, and 0.1. For the sake of clarity, we have chosen the electronic band structure for three different doping cases as shown on Figure 3.1, and the spin splitting of bands is evident from this figure and Figure 3.2 (a). Due to strong SOI and since BiTeI lacks inversion symmetry, the degenerate electronic bands are lifted except at $k = 0$ point, which is protected by time invariance symmetry. As can be seen from Figure 3.1 (a), E_F is located at the middle of CBM and VBM when neither electrons nor holes are doped to the system. This is in consistent with the semiconductor property of BiTeI: i.e., for a typical intrinsic semiconductor, the Fermi energy is located in between CBM and VBM at zero temperature. When n_e=-0.1 is doped to BiTeI, E_F is shifted to the conduction band as shown in Figure 3.1 (b). More specifically, it is located above the crossing point. Note that, bands that fall below E_F are full of electrons, and in this case the system is metallic because electrons are present in the conduction bands in addition to the valance bands. In the case of hole doping as shown in Figure 3.1 (c), when n_e=+0.1 is doped to BiTeI, E_F is moving down to the valance band. The displacement of E_F with n_e is in agreement with rigid band approximation, and similar results are found to the rest of electronic band structures which are not shown here.

The curvature of the band within 2 eV of E_F at the Gamma point is flat compared to other high symmetric points. Therefore, this region has high electron density which facilitate EPI. Table I shows the band gap at four different high symmetric points as a function of three doping concentration, namely, n_e=0.00, -0.1, and +0.1. Comparing the second, third, and fourth column of Table 3.1, one can see that the band gap at M and H decreasing while it is increasing and stays constant at Γ and A, respectively. Even though we have not calculated the transition matrix element for the possible optical transitions in these band

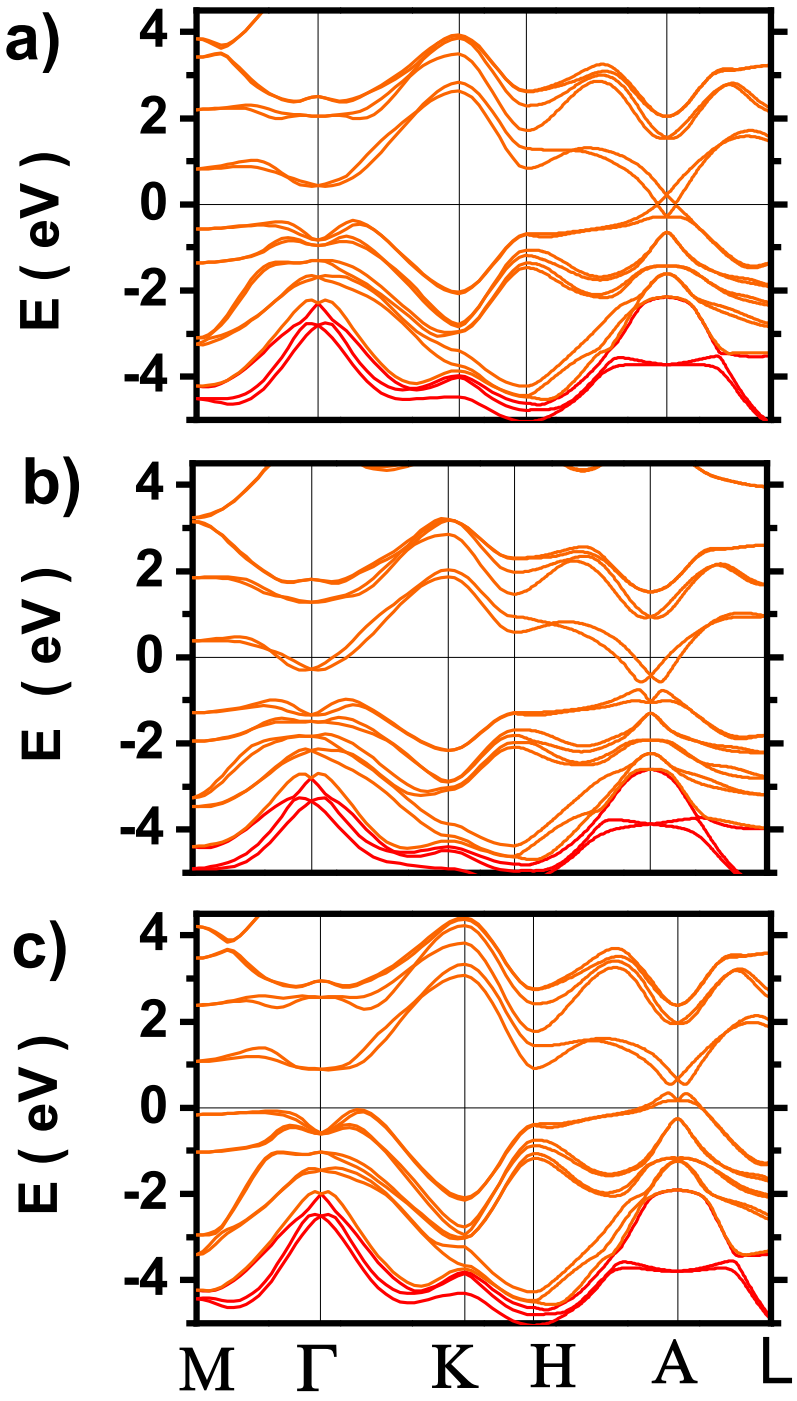

Figure 3.1: Electronic band structure of BiTeI at three different carrier concentration. (a) n_e=0.0 (Undeoped BiTeI), where E_F is located exactly in the middle of CBM and VBM. (b) n_e=-0.1 doped BiTeI, where E_F is shifted towards the conduction band. (c) n_e=0.1, where E_F is shifted towards the valance band.

Table 3.1: Band gap of BiTeI at four high symmetric points for n_e=0.00, -0.1, and 0.1.

E_g (eV)	n_e=-0.1	n_e=0.00	n_e=0.1
M	1.473	1.397	1.238
Γ	1.059	1.274	1.475
H	1.867	1.516	1.300
A	0.603	0.497	0.483

gaps, it is good to talk about qualitatively about this phenomena.

There are possible optical transitions at M, G, H, and A points in the infrared regime. Because, the wavelength associated with the energy gap lies within 0.7-10 μm, which is the energy range of infrared electromagnetic specturum. However, at H point of n_e=-0.1 the band gap energy is 1.867 eV, and its wavelength ($664nm$) is smaller than the infrared regime. Therefore, the optical transition in this case is that of visible light. Doping BiTeI with electrons and holes minimally alter the optical transition energy. Out of the four high symmetric points, A has the smallest band gap energy as shown on the last row Table 3.1. We have noticed a band gap closing and opening phenomena at the A point for electron doping when the concentration of free carriers are increasing. Note that, what we mean by A point is to the right of it; because of the Rashba SOI, the CBM and VBM of the spin-splitting bands are found to be shifted from A. The minimum band gap (band closing) of 8 meV is observed when BiTeI is doped with 0.025 electron. Hence, BiTeI is transformed from semiconductor to semi-metal at n_e=0.025. Moreover, it is a direct band gap at the A point since the change in momentum is negligibly small at this point.

3.3.2 Variation of Rashba energy, momentum, and parameter under electron and hole doping

The Rashba energy, momentum, and parameter are related with each other by a simple mathematical formula, α_R=2E$_R$/K$_R$. Where α_R, E$_R$, and K$_R$ are Rashba parameter, Rashba energy, and Rashba momentum, respectively. Figure 3.2 depicts the behaviour of these quantities under electron and hole doping for the valance and conduction bands indicated as v and c on the superscript notation, respectively. The Rashba energy for the conduction

band (E_R^c) is defined as the energy difference between the CBM and crossing point-the point at which the spin-splitting bands cross each other, whereas the Rashba energy for the valance band (E_R^v) is defined as the energy difference between the VBM and crossing point. Similarly, the Rashba momentum for the conduction band (K_R^c) is defined as the momentum difference between the CBM and crossing point, whereas the Rashba momentum for the valance band (K_R^v) is defined as the momentum difference between the VBM and crossing point. These definitions are shown schematically in Figure 3.2 (a).

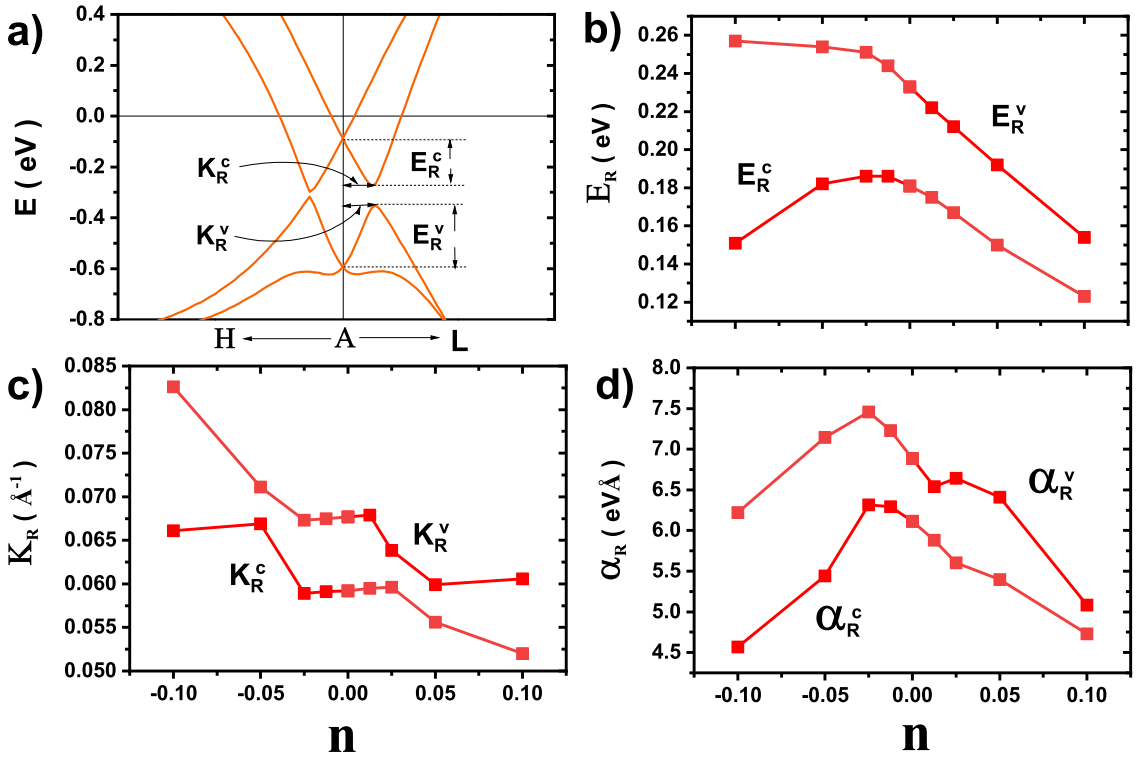

Figure 3.2: Rashba energy, Rashba momentum, and Rashba parameter at different n_e. (a) The definition of Rashba energy and Rashba momentum for the valance and conduction bands along H-A-L direction. (b) Rashba energy as a function of n_e. (c) Rashba momentum as a function of n_e. (d) Rashba parameter as a function of n_e. The maximum of α_R^v and α_R^c occurred at n_e=-0.025.

As depicted in Figure 3.2 (b), E_R^v and E_R^c resemble similar behavior for hole doping: both of them decrease monotonically from n_e=0.00 to n_e=0.1. However, they show quite different

behavior for electron doping, specially after n_e=-0.025; E_R^v increases for electron doping, whereas E_R^c increases up to n_e=-0.025 and it decreases sharply afterwards. Furthermore, ΔE_R^v is increased by 103 meV (40%) from n_e=0.1 to n_e=-0.1, and ΔE_R^c is increased by 63 meV (34%) from n_e=0.1 to n_e=-0.0125. Therefore, Rashba energy is significantly tuned by the application of electrostatic doping. K_R^v and K_R^c are constant from n_e=0.0125 to n_e=-0.025, which are shown clearly in Figure 3.2 (c). However, ΔK_R^v from n_e=-0.025 to n_e=-0.1 is increased by 0.0153 $\mathring{A}^{-1}$, and ΔK_R^c from n_e=0.1 to n_e=0.025 is increased by 0.0076 $\mathring{A}^{-1}$. In general, ΔE_R^v is greater than ΔE_R^c and ΔK_R^v is greater than ΔK_R^c.

The Rashba parameters for conduction and valance band have extrema as illustrated on Figure 3.2 (d) at n_e=-0.025. Since the spin splitting of CBM and VBM is due to the second order perturbative correction in energy of the k.p model, the band gap must have a minimum value at this electron concentration [113]. This is indeed confirmed in our result and depicted in Figure 3.3. More specifically, the minimum value of the band gap is 8 meV. The maximum values of α_R^v and α_R^c are 7.46 and 6.32 eV$\mathring{A}$, respectively. $\alpha_R^v = 7.46$ eV$\mathring{A}$ is the largest value that we have noticed so far. Moreover, $\Delta\alpha_R^v$ is increased by 2.38 eV$\mathring{A}$ (31%) from n_e=0.1 to n_e=-0.025 while $\Delta\alpha_R^c$ is increased by 1.59 eV$\mathring{A}$ (25%) from n_e=0.1 to n_e=-0.025. To the right and left of the maxima, both α_R^v and α_R^c are decreasing sharply as the concentration of holes and electrons are increasing, respectively. The Rashba energy, momentum, and parameter are larger for valance band(hole) than conduction band (electron). Therefore, BiTeI could be a potential candidate for hole-based spintronics device. However, it can also be used for a p-n junction transistors since both electrons and holes are involved in the transport properties of semiconductors.

Doping a material with electron causes a volume expansion, whereas doping a material with holes causes a volume contraction [32, 58, 74, 114]. This phenomena is indeed confirmed in our result. Figure 3.3 (a) and (b) shows that electron doping increases the lattice vector a and c, however, hole doping decreases both of them. Hence, the presence of strong SOI in BiTeI does not influence the change of volume with respect to doping. The band gap closing

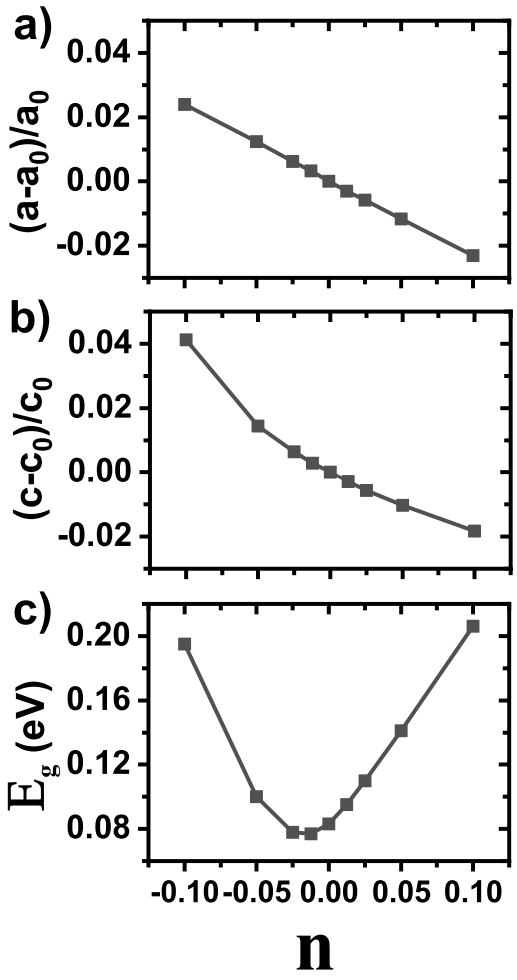

Figure 3.3: Strain and band gap for hole and electron doping. (a) In-plane strain against n_e; (b) Out of plane strain against n_e. (c) Band gap against n_e. The minimum of the band gap which is 8 meV occurs at n_e=-0.025.

and opening phenomena is clearly illustrated in Figure 3.3 (c). The band gap increases for hole doping while it decreases with a minimum value of 8 meV and then increases for electron doping.

3.3.3 Electron phonon coupling constant (λ) under electron and hole doping

The electron phonon coupling constant (λ) is mostly used to determine the transition temperature of superconductors by using semiempirical McMillan formula [115]. We have calculated λ for different values of energy corresponding to E_F as shown on Figure 3.4. Since the effect of electron or hole doping on E_F is to shift its original value up or down in the conduction or valance band respectively, we have used the electronic band structure of n_e=-0.0125 doped BiTeI and vary only the value of the energy. Figure 3.4 (a) shows the electronic band structure of n_e=-0.0125 doped BiTeI together with the values of energies (E_F) used to compute λ. These are E_1= 5.15, E_2= 5.275, E_3= 5.4, E_4= 5.5, and E_5= 5.6 eV for the conduction band, and $E_1^{'}$= 4.95, $E_2^{'}$= 4.8, $E_3^{'}$= 4.7, $E_4^{'}$= 4.6, and $E_5^{'}$= 4.5 eV for the valance band. The density of state (DOS), which is useful to understand λ is depicted in Figure 3.4 (b). Figure 3.4 (c) and (d) show λ as a function of $E-E_{CBM}$ and $E-E_{VBM}$, respectively. E_{CBM} and E_{VBM} are 5.095 and 5.018 eV, respectively. In the following paragraphs we discuss in detail the behavior of λ for both electron and hole doping.

Surprisingly, λ has very different characteristics for electron and hole doping as shown on Figure 3.4 (c) and (d), respectively. For electron doping, λ starts to decrease from E_1 to E_2 and then it increases from E_3 to E_5. Hence, λ vs $E-E_{CBM}$ graph has some type of bell shaped structure with a minimum value of 0.05. For hole doping, however, λ increases monotonically as the concentration of holes increase. The behavior of λ can easily be understood using Figure 3.4 (b). Generally speaking, λ increases with DOS, i.e., large value of DOS corresponding to large value of λ except when the energy (E_F) is near to the crossing point, and in this case the superconductivity is low. This is applied for electron doping only. For example, the energies located in between E_2 and E_3 are near to the crossing

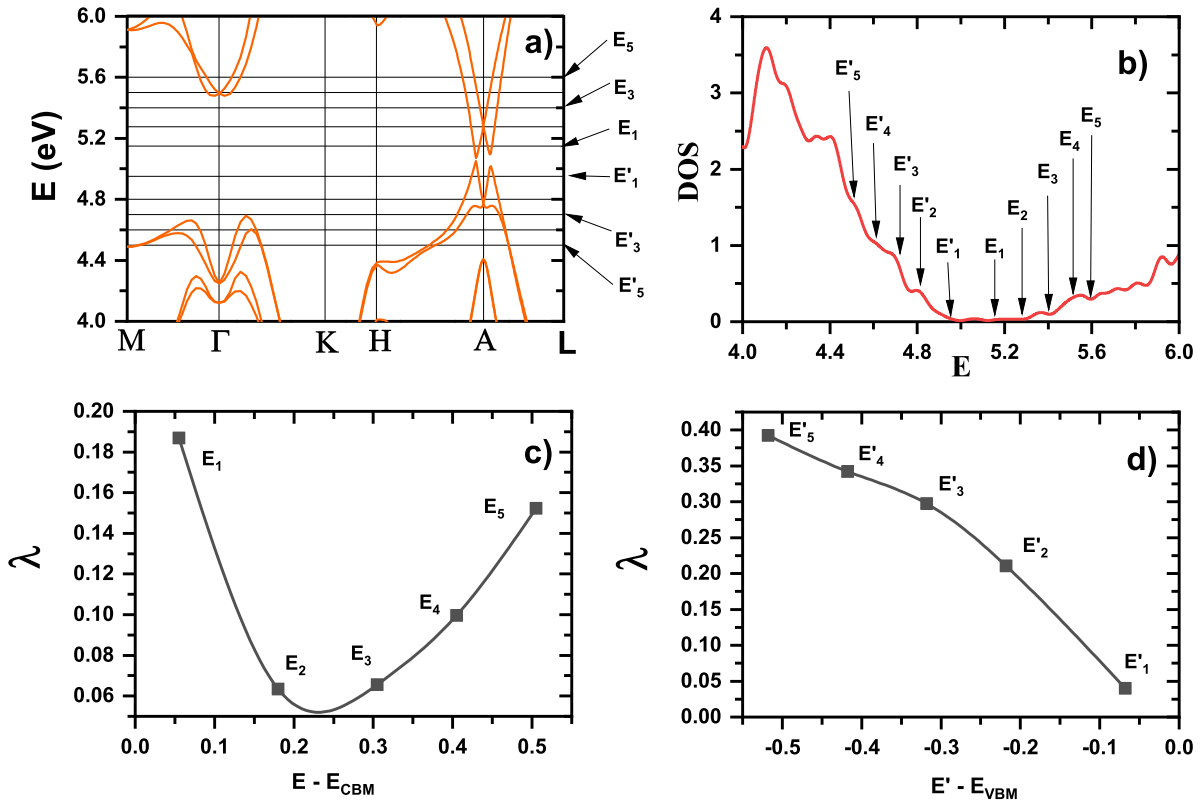

Figure 3.4: Electron phonon coupling constant (λ) under electron and hole doping. (a) Electronic band structure of n_e=-0.0125 doped BiTeI within 4-6 eV. The values of energy corresponding to E_F are shown with prime superscript for valance band and without prime superscript for conduction bands. (b) Density of state(DOS) of the aforementioned band structure. (c) λ vs $E-E_{CBM}$, where E_{CBM} is the energy of conduction band minimum. (d) λ vs E_{VBM}, where E_{VBM} is the energy of valance band maximum.

point of the conduction band and their λ are small (the existence of minima on Figure 3.4 (c)) compared with E_1, E_4, and E_5, which are a bit far from the crossing point.

The maximum value of λ for hole doping employing anisotropic Eliashberg equations from EPW module is 0.46, which corresponds to $E_5^{'}$= 4.5 eV. Furthermore, the estimated Allen-Dynes critical temperature, logarithmic frequency (ω_{log}), and BSC superconducting gap are 0.7 K, 7 meV, and 0.1 meV, respectively. The critical temperature (T_C) is calculated with a Coulomb pseudopotential of 0.1. The value of T_C is somehow small, however, λ of BiTeI is comparable to Al and Mo. Note that, we have not included the polar characteristics of BiTeI when we compute λ. Hence, we expect λ to be different from what we have found if this property is incorporated in the EPI by the flag lpolar = true, which take into account the long-range contribution to the electron-phonon matrix element.

3.4 Conclusions

In this paper, we have extensively investigated the effect of electron and hole doping on the spin-splitting of valance and conduction bands in BiTeI, which is characterized by the Rashba energy, Rashba momentum, and Rashba parameter. Furthermore, we have studied the same effect on the e-ph coupling constant (λ) of BiTeI. These quantities can be tuned in a wide range of values using doping (electrons and holes) as a parameter. ΔE_R^v is increased by 103 meV (40%) from n_e=0.1 to n_e=-0.1, and ΔE_R^c is increased by 63 meV (34%) from n_e=0.1 to n_e=-0.0125. However, ΔK_R^v from n_e=-0.025 to n_e=-0.1 is increased by 0.0153 $\mathring{A}^{-1}$, and ΔK_R^c from n_e=0.1 to n_e=0.025 is increased by 0.0076 $\mathring{A}^{-1}$. α_R^v and α_R^c has maximum value of 7.46 and 6.32 eV$\mathring{A}$, respectively. α_R^v = 7.46 eV$\mathring{A}$ is the largest value that we came across in any literature review. Moreover, $\Delta\alpha_R^v$ is increased by 2.38 eV$\mathring{A}$ (31%) from n_e=0.1 to n_e=-0.025 while $\Delta\alpha_R^c$ is increased by 1.59 eV$\mathring{A}$ (25%) from n_e=0.1 to n_e=-0.025. In general, $E_R^V > E_R^c$, $K_R^V > K_R^c$, and $\alpha_R^v > \alpha_R^c$. Therefore, BiTeI could be used for hole-based spintronics device. λ of electrons is completely unique than holes. The former one has a minima while the later one increase monotonically as the concentration of holes increase. The calculated

value of λ corresponding to $E_5^{'}$= 4.5 eV is 0.46, and its associated T_C is 0.7K. These values are very small to be used for practical application, and further study is necessary to better understand potential superconductivity characteristics of BiTeI.

4 Summary and Outlook

Polar-metals could be artificially created using doping as a mechanism of tuning the electric and vibrational properties of ferroelectrics. Centrosymmetric tetragonal $PbTiO_3$ has ferroelectric instability (existence of soft modes) at the Γ point, and surprisingly this instability persist up to an electron concentration of n=0.7 e/u.c (electron per unit cell). Electron doping significantly changes the normal modes of vibration and enhances mode interaction and mixing; strong mode-mode interaction between $A_{2u}(TO_1)$ and $A_{2u}(TO_2)$ is the primary reason why we have the persistence of soft modes at high electron doping. As a result, metallicity and ferroelectricity coexist in an electron doped $PbTiO_3$. The polarity is due to the presence of ferroelectric instability and the metallicity is due to the charge carries introduced in the system by doping. Despite the long range Coulomb interaction is affected by the free electron, the existence of ferroelectric instability supports the idea that the short range interaction (particularly the Pb-O interaction) is the predominant factor of developing ferroelectricity in highly-doped $PbTiO_3$. However, in undoped $PbTiO_3$, the ferroelectricity is due to Ti-O interaction. In $BaTiO_3$, the interaction between $A_{2u}(TO_1)$ and $A_{2u}(TO_2)$ is very weak that the ferroelectric instability cease to exist at a critical electron concentration of n=0.14 e/u.c. We belive that mode-mode interaction is a universal phenomena and it can be generalized to other ferroelectric materials. Therefore, our results give important insight about polar-metal characteristics of electron doped $PbTiO_3$ and may be useful in terms of opening future investigation to utilize this material for novel applications, such as capacitors, superconductors, and photovolatics, .

Strain is as important as doping to tune the physical and chemical properties of *perovskite* oxides. Perovskite oxides are a class of ferroelectric materials which have ABO_3 chemical formula. A can be monovalent or divalent cation and B can be tetravalent or pentavalent metal. Therefore, it would be advantageous to use both to find a useful material that can operate at room temperature. $PbTiO_3$ is a well known perovskite ferroelectric material. Doping

$PbTiO_3$ with Nb changes it from ferroelectric to metal. Since Nb has five valance electrons, substituting Ti (which has four valance electrons) by Nb in $PbTiO_3$ leads to one extra electron. The double potential well of Nb-doped $PbTiO_3$ has a minimum energy of -0.095 meV, which is unstable under ambient temperature ($K_BT \sim 25$ meV). To overcome this condition 1%, 2%, and 3% an in-plane compressive strain is applied to Nb-doped $PbTiO_3$, and the minimum energy is shifted to -18.3, -29.5, and -39.7 meV, respectively. Therefore, $PbTiO_3$ transforms from metal to polar-metal. More specifically, it is now a room temperature polar metal ($K_BT \sim 25$ meV < 29.5 and 39..7 meV).

BiTeI is a non-centrosymmetric semiconductor with a band gap of 0.3 eV when spin-orbit(SO) interaction is included. The spin-splitting of bands in systems that lack an inversion symmetry due to strong SO interaction leads to many novel physical phenomena in which spin Hall effect and superconductivity are two of them. Doping BiTeI with electrons and holes change significantly not only the Rashba energy, momentum, and parameter but also the electron-phonon coupling constant (λ). ΔE_R^v is increased by 103 meV from n_e=0.1 to n_e=-0.1, and ΔE_R^c is increased by 63 meV from n_e=0.1 to n_e=-0.0125. Similarily, $\Delta\alpha_R^v$ is increased by 2.38 eV$\mathring{A}$ from n_e=0.1 to n_e=-0.025 while $\Delta\alpha_R^c$ is increased by 1.59 eV$\mathring{A}$ from n_e=0.1 to n_e=-0.025. Furthermore, the Rashba parameters for conduction and valance band have extrema value of 7.46 and 6.32 eV$\mathring{A}$, respectively at n_e=-0.025. Most values Rashba parameters in a literature are less than our findings. Therefore, our results are unique and yet to be verified by experiment. λ of electrons has a minima while for holes it increases monotonically with the concentration of holes. The calculated critical temperature (T_C = 0.7K) is very small for practical application, and our study open up future investigation to increase this value.

The followings are main research questions for future work:

* How to increase the efficiency of a memory device from the usual perovskite oxides of the form ABO_3 by using chemical or charge doping?

* While changing ferroelectrics into polar-metals employing structural constraints (natu-

ral method) and chemical or charge doping (artificial method), which families of ferroelectrics could have feasible application for superconductivity?

* How can one increase the critical temperature of Rashba type semiconductors (BiTeI, BiTeBr, and BiTeCl) and non-centrosymmetric superconductor ($CePt_3Si$) employing chemical or charge doping and without the application of pressure?

A Copyright Information

Copyright policies of the American Physical Society (APS)

American Physical Society
Reuse and Permissions License

21-Jul-2022

This license agreement between the American Physical Society ("APS") and Zegnet Muhammed ("You") consists of your license details and the terms and conditions provided by the American Physical Society and SciPris.

Licensed Content Information

License Number:	**RNP/22/JUL/055951**
License date:	21-Jul-2022
DOI:	10.1103/PhysRevB.101.174105
Title:	Origin of the persistence of soft modes in metallic ferroelectrics
Author:	Zegnet Yimer and Huaxiang Fu
Publication:	Physical Review B
Publisher:	American Physical Society
Cost:	USD $ 0.00

Request Details

Does your reuse require significant modifications: No

Specify intended distribution locations:	United States
Reuse Category:	Reuse in a thesis/dissertation
Requestor Type:	Student
Items for Reuse:	Whole Article
Format for Reuse:	Electronic

Information about New Publication:

University/Publisher:	University of Arkansas
Title of dissertation/thesis:	First-Principles Study of Doping Effects on Ferroelectricity and on Rashba Spin Splitting
Author(s):	Zegnet Yimer Muhammed
Expected completion date:	Jul. 2022

License Requestor Information

Name:	Zegnet Muhammed
Affiliation:	Individual
Email Id:	zymuhamm@uark.edu
Country:	United States

B Band structure comparison of QE and EPW

Comparison of the electronic band structure of n_e=-0.0125 doped BiTeI with QE and EPW. The EPW band structure is the same as QE. Therefore, the calculation we have performed to find different physical quantities describing superconductivity is accurate. The same initial projections are used to compute maximally-localized Wannier functions (MLWF) for Bi, Te, and I. These are S, P, and d_{Z^2} orbitals.

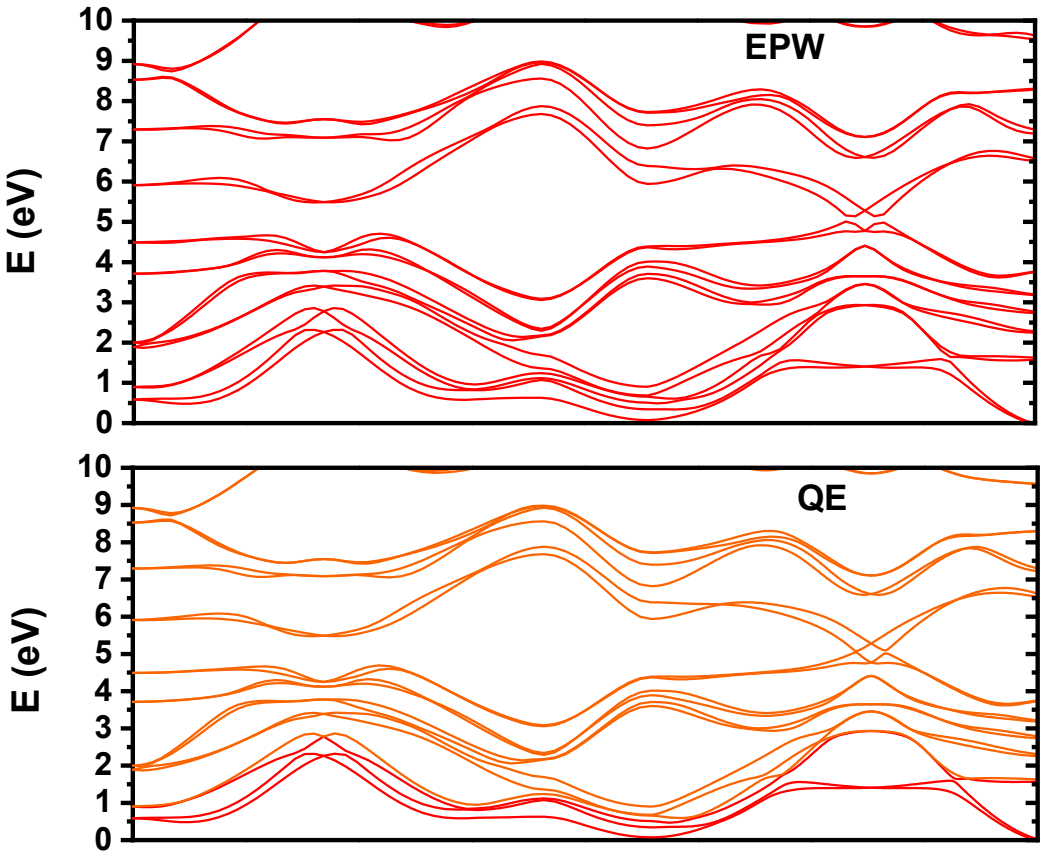

C Determination of convergence criteria for the fine nkf1 mesh

The electron phonon coupling constant (λ) versus nkf1 is shown on the figure below for fixed nqf1×nqf2×nqf3 = 8×8×4, and λ is converged for nkf1 = 60. Hence, nkf1×nkf2 = 60×60 are chosen due to the symmetry of BiTeI crystal structure; the in-plane lattice vectors are equal (a=b) for trigonal BiTeI. Therefore, nkf1 = nkf2.

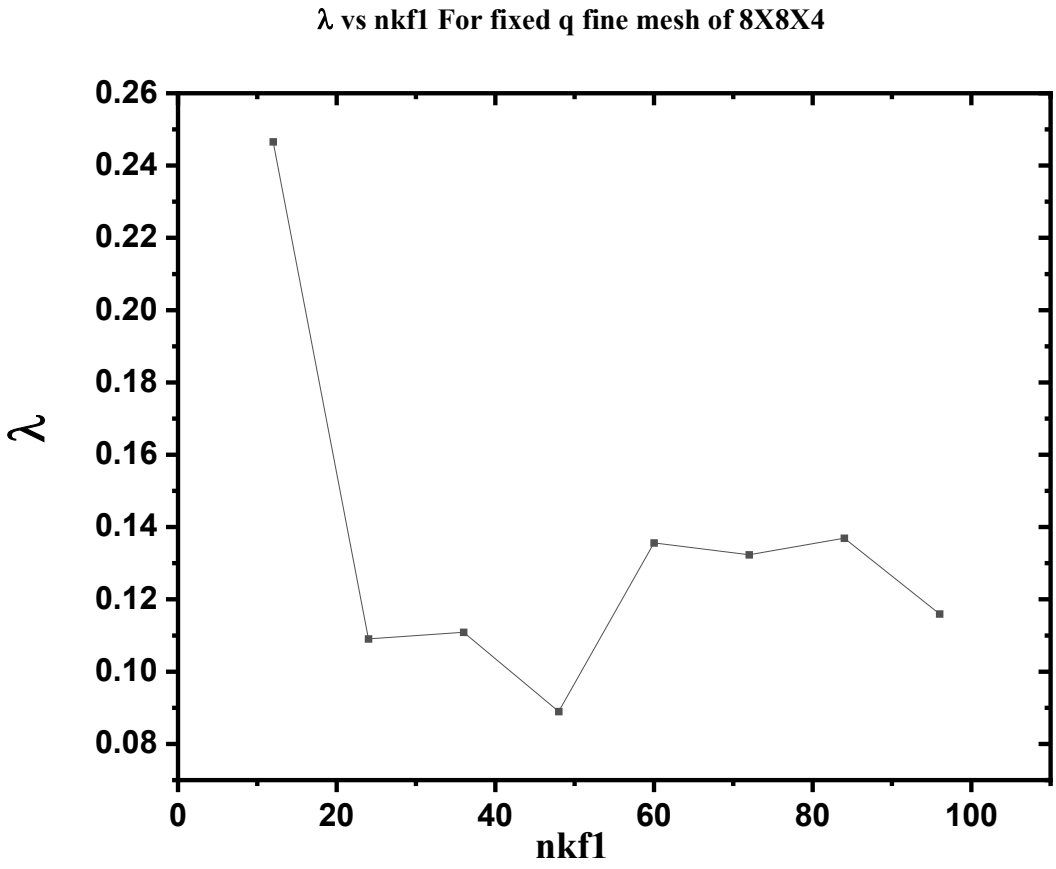

D Determination of convergence criteria for the fine nkf3 mesh

The electron phonon coupling constant (λ) versus nkf3 is shown on the figure below for fixed nqf1×nqf2×nqf3 = 8×8×4, and λ is converged for nkf3 = 50. Hence, nkf1×nkf2×nkf3 = 60×60×48 are chosen to determine nqf1×nqf2×nqf3.

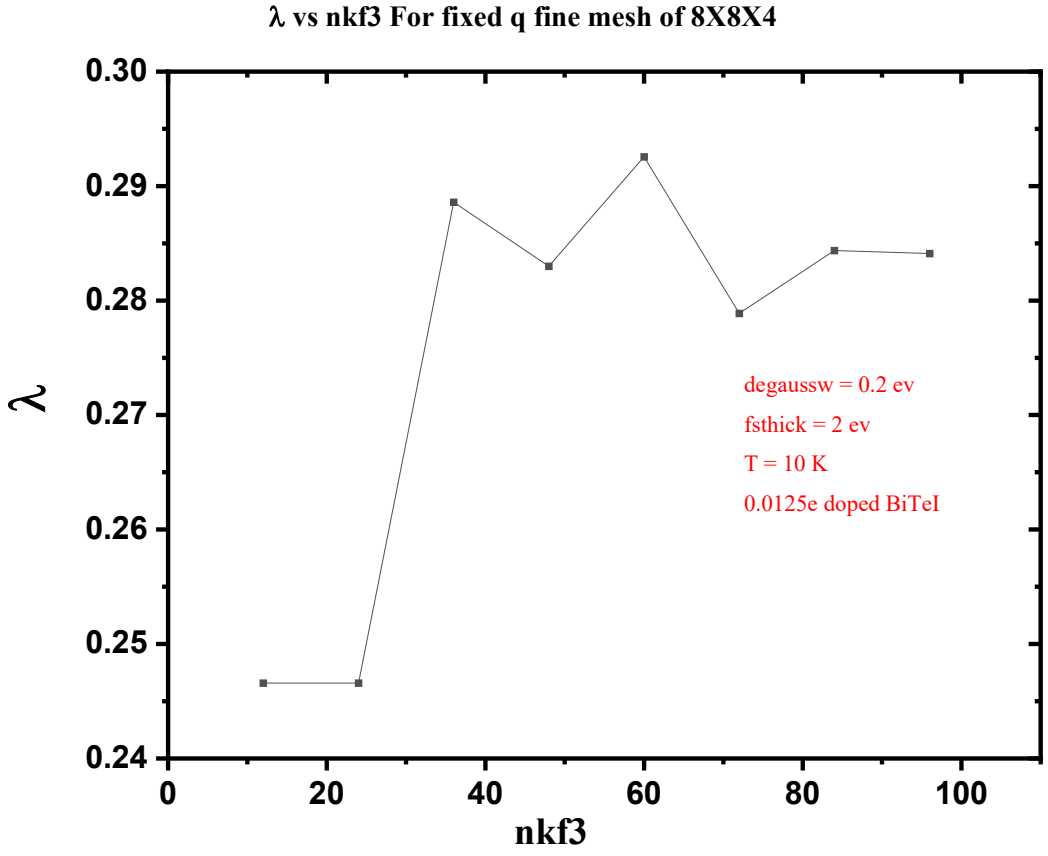

E Determination of convergence criteria for the fine nqf1 mesh

The electron phonon coupling constant (λ) versus nqf1 is shown on the figure below for fixed nkf1×nkf2×nkf3 = 12×12×12, and λ is converged for nqf1 = 12. Hence, nqf1×nqf2 = 12×12 are chosen due to the symmetry of BiTeI crystal structure.

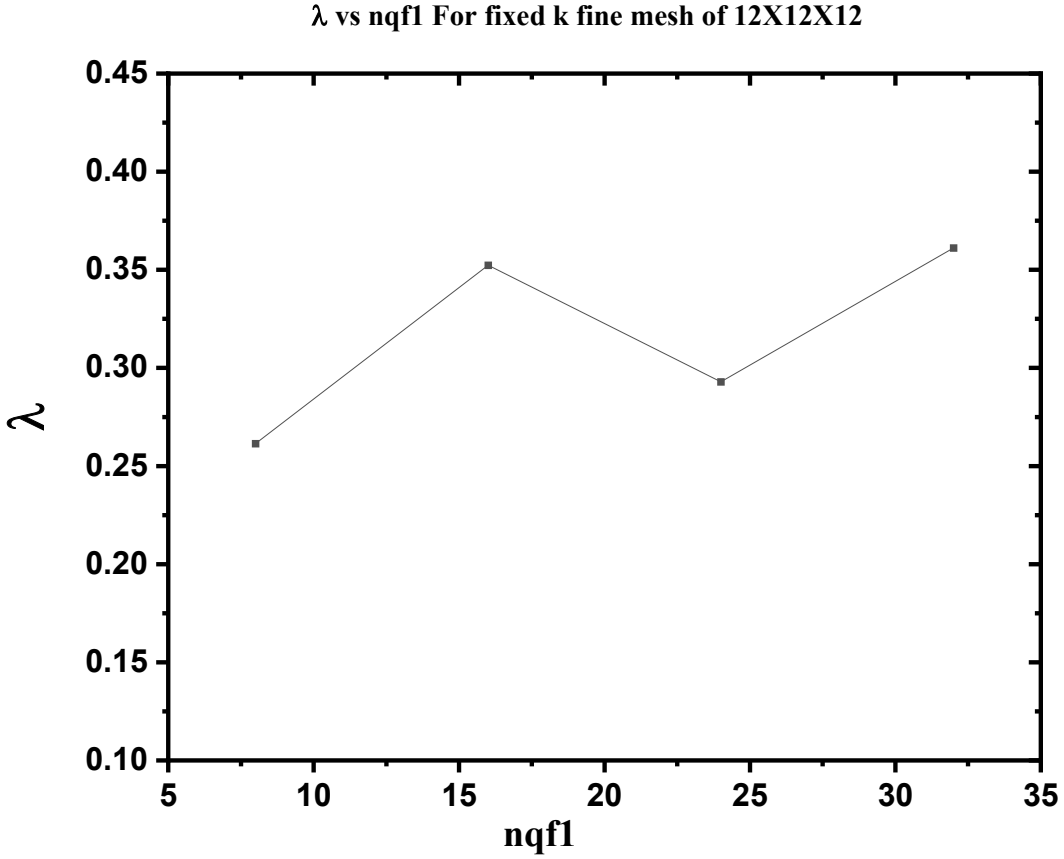

F Determination of convergence criteria for the fine nqf3 mesh

The electron phonon coupling constant (λ) versus nqf3 is shown on the figure below for fixed nkf1×nkf2×nkf3 = 12×12×12, and λ is converged for nqf3 = 8. Hence, nqf1×nqf2×nqf3 = 12×12×8 are chosen to compute the superconducting properties of BiTeI.

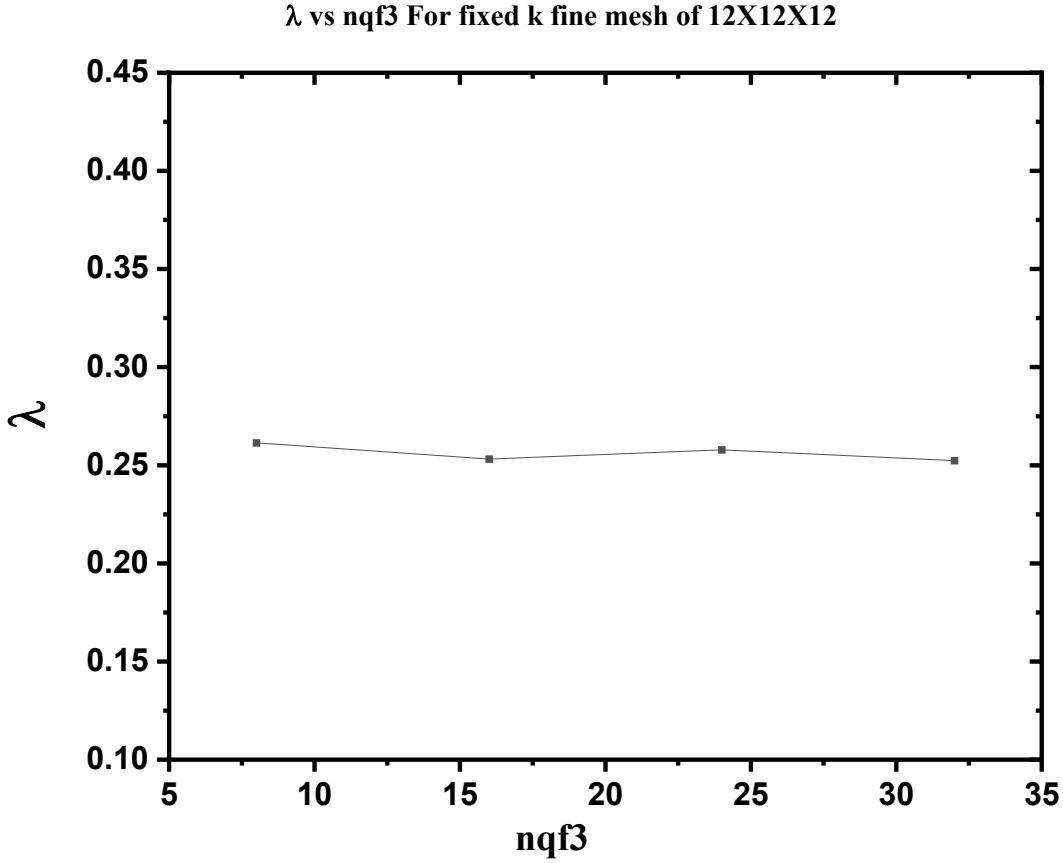

Bibliography

[1] P. W. Anderson and E. Blount, Physical Review Letters **14**, 217 (1965).

[2] T. Kim, D. Puggioni, Y. Yuan, L. Xie, H. Zhou, N. Campbell, P. Ryan, Y. Choi, J.-W. Kim, J. Patzner, et al., Nature **533**, 68 (2016).

[3] R. E. Cohen, Nature **358**, 136 (1992).

[4] R. Cohen and H. Krakauer, Physical Review B **42**, 6416 (1990).

[5] W. Cochran, Advances in Physics **9**, 387 (1960).

[6] M. E. Lines and A. M. Glass, *Principles and applications of ferroelectrics and related materials* (Oxford university press, 2001).

[7] J. G. Bednorz and K. A. Müller, Zeitschrift für Physik B Condensed Matter **64**, 189 (1986).

[8] D. C. Tsui, H. L. Stormer, and A. C. Gossard, Physical Review Letters **48**, 1559 (1982).

[9] M. Dawber, K. Rabe, and J. Scott, Reviews of modern physics **77**, 1083 (2005).

[10] S.-E. Park and T. R. Shrout, Journal of applied physics **82**, 1804 (1997).

[11] H. Fu and R. E. Cohen, Nature **403**, 281 (2000).

[12] B. Noheda, D. Cox, G. Shirane, S.-E. Park, L. Cross, and Z. Zhong, Physical Review Letters **86**, 3891 (2001).

[13] X. Fu, I. I. Naumov, and H. Fu, Nano letters **13**, 491 (2013).

[14] A. George, J. Iniguez, and L. Bellaiche, Nature **413**, 54 (2001).

[15] J. Neaton and K. Rabe, Applied Physics Letters **82**, 1586 (2003).

[16] I. I. Naumov, L. Bellaiche, and H. Fu, Nature **432**, 737 (2004).

[17] I. I. Naumov and H. Fu, Physical review letters **101**, 197601 (2008).

[18] C. J. Fennie and K. M. Rabe, Physical Review B **72**, 100103 (2005).

[19] E. Bousquet, M. Dawber, N. Stucki, C. Lichtensteiger, P. Hermet, S. Gariglio, J.-M. Triscone, and P. Ghosez, Nature **452**, 732 (2008).

[20] N. A. Benedek and C. J. Fennie, Physical review letters **106**, 107204 (2011).

[21] J. M. Rondinelli and C. J. Fennie, Advanced Materials **24**, 1961 (2012).

[22] D. Puggioni, G. Giovannetti, and J. M. Rondinelli, Journal of Applied Physics **124**, 174102 (2018).

[23] V. M. Edelstein, Physical Review B **83**, 113109 (2011).

[24] V. Mineev and Y. Yoshioka, Physical Review B **81**, 094525 (2010).

[25] V. M. Edelstein, Physical review letters **75**, 2004 (1995).

[26] E. U. Condon, in *Selected Scientific Papers of EU Condon* (Springer, 1991), pp. 306–348.

[27] Y. Shi, Y. Guo, X. Wang, A. J. Princep, D. Khalyavin, P. Manuel, Y. Michiue, A. Sato, K. Tsuda, S. Yu, et al., Nature materials **12**, 1024 (2013).

[28] G. Giovannetti and M. Capone, Physical Review B **90**, 195113 (2014).

[29] H. Xiang, Physical Review B **90**, 094108 (2014).

[30] D. Puggioni, G. Giovannetti, M. Capone, and J. M. Rondinelli, Physical review letters **115**, 087202 (2015).

[31] N. A. Benedek and T. Birol, Journal of Materials Chemistry C **4**, 4000 (2016).

[32] H. J. Zhao, A. Filippetti, C. Escorihuela-Sayalero, P. Delugas, E. Canadell, L. Bellaiche, V. Fiorentini, and J. Íñiguez, Physical Review B **97**, 054107 (2018).

[33] D. Puggioni and J. M. Rondinelli, Nature communications **5**, 1 (2014).

[34] P. Hohenberg and W. Kohn, Physical review **136**, B864 (1964).

[35] W. Kohn and L. J. Sham, Physical review **140**, A1133 (1965).

[36] P. Giannozzi, S. Baroni, N. Bonini, M. Calandra, R. Car, C. Cavazzoni, D. Ceresoli, G. L. Chiarotti, M. Cococcioni, I. Dabo, et al., Journal of physics: Condensed matter **21**, 395502 (2009).

[37] P. Giannozzi, S. Baroni, N. Bonini, M. Calandra, R. Car, C. Cavazzoni, D. Ceresoli, G. L. Chiarotti, M. Cococcioni, I. Dabo, et al., Journal of Physics: Condensed Matter **21**, 395502 (19pp) (2009), URL http://www.quantum-espresso.org.

[38] N. Troullier and J. L. Martins, Physical review B **43**, 1993 (1991).

[39] H. Fu and O. Gülseren, Physical Review B **66**, 214114 (2002).

[40] Z. Alahmed and H. Fu, Physical Review B **76**, 224101 (2007).

[41] S. Baroni, S. De Gironcoli, A. Dal Corso, and P. Giannozzi, Reviews of modern Physics **73**, 515 (2001).

[42] S. Baroni, P. Giannozzi, and A. Testa, Physical review letters **58**, 1861 (1987).

[43] X. Gonze, Physical Review A **52**, 1096 (1995).

[44] A. Raeliarijaona and H. Fu, Physical Review B **92**, 094303 (2015).

[45] C. Ederer and N. A. Spaldin, Physical review letters **95**, 257601 (2005).

[46] A. García and D. Vanderbilt, Physical Review B **54**, 3817 (1996).

[47] Y. Yao and H. Fu, Physical Review B **84**, 064112 (2011).

[48] J. Ribeiro-Soares, R. Almeida, E. B. Barros, P. T. Araujo, M. S. Dresselhaus, L. G. Cançado, and A. Jorio, Physical Review B **90**, 115438 (2014).

[49] P. Ghosez, E. Cockayne, U. Waghmare, and K. Rabe, Physical Review B **60**, 836 (1999).

[50] N. Ashcroft and N. Mermin, *Solid State Physics* (Saunders College, 1976).

[51] A. Ohtomo and H. Hwang, Nature **427**, 423 (2004).

[52] J. Slater, Physical Review **78**, 748 (1950).

[53] J. Hlinka and J. Petzelt, Phase Transitions **79**, 41 (2006).

[54] J. T. Last, Physical Review **105**, 1740 (1957).

[55] W. Zhong, R. King-Smith, and D. Vanderbilt, Physical review letters **72**, 3618 (1994).

[56] D. Eagles, Journal of Physics and Chemistry of Solids **25**, 1243 (1964).

[57] N. Laurita, A. Ron, J.-Y. Shan, D. Puggioni, N. Koocher, K. Yamaura, Y. Shi, J. Rondinelli, and D. Hsieh, Nature communications **10**, 1 (2019).

[58] X. He and K.-j. Jin, Physical Review B **94**, 224107 (2016).

[59] C. Paillard, E. Torun, L. Wirtz, J. Íñiguez, and L. Bellaiche, Physical Review Letters **123**, 087601 (2019).

[60] S. Ghosh, A. Y. Borisevich, and S. T. Pantelides, Physical Review Letters **119**, 177603 (2017).

[61] J. Fujioka, D. Okuyama, D. Morikawa, T. Arima, K. Okada, Y. Kaneko, T. Fukuda, H. Uchiyama, D. Ishikawa, A. Baron, et al., Scientific reports **5**, 1 (2015).

[62] Z. Fei, W. Zhao, T. A. Palomaki, B. Sun, M. K. Miller, Z. Zhao, J. Yan, X. Xu, and D. H. Cobden, Nature **560**, 336 (2018).

[63] S. Lee, J. A. Bock, S. Trolier-McKinstry, and C. A. Randall, Journal of the European Ceramic Society **32**, 3971 (2012).

[64] J. M. Rondinelli and C. J. Fennie, Advanced Materials **24**, 1918 (2012).

[65] Z. Chen, A. G. Swartz, H. Yoon, H. Inoue, T. A. Merz, D. Lu, Y. Xie, H. Yuan, Y. Hikita, S. Raghu, et al., Nature communications **9**, 1 (2018).

[66] K. J. Choi, M. Biegalski, Y. Li, A. Sharan, J. Schubert, R. Uecker, P. Reiche, Y. Chen, X. Pan, V. Gopalan, et al., Science **306**, 1005 (2004).

[67] J. Wang, J. Neaton, H. Zheng, V. Nagarajan, S. Ogale, B. Liu, D. Viehland, V. Vaithyanathan, D. Schlom, U. Waghmare, et al., science **299**, 1719 (2003).

[68] D. G. Schlom, L.-Q. Chen, C.-B. Eom, K. M. Rabe, S. K. Streiffer, and J.-M. Triscone, Annu. Rev. Mater. Res. **37**, 589 (2007).

[69] D. G. Schlom, L.-Q. Chen, C. J. Fennie, V. Gopalan, D. A. Muller, X. Pan, R. Ramesh, and R. Uecker, Mrs Bulletin **39**, 118 (2014).

[70] G. A. Rossetti Jr, L. E. Cross, and K. Kushida, Applied physics letters **59**, 2524 (1991).

[71] R. Adhikari and H. Fu, Journal of Applied Physics **116**, 123712 (2014).

[72] J. Haeni, P. Irvin, W. Chang, R. Uecker, P. Reiche, Y. Li, S. Choudhury, W. Tian, M. Hawley, B. Craigo, et al., Nature **430**, 758 (2004).

[73] K. Kushida and H. Takeuchi, Ferroelectrics **108**, 3 (1990).

[74] Y. Iwazaki, T. Suzuki, Y. Mizuno, and S. Tsuneyuki, Physical Review B **86**, 214103 (2012).

[75] Z. Yimer and H. Fu, Physical Review B **101**, 174105 (2020).

[76] K. Takahashi, Y. Matsubara, M. Bahramy, N. Ogawa, D. Hashizume, Y. Tokura, and M. Kawasaki, Scientific reports **7**, 1 (2017).

[77] J.-x. Gu, K.-j. Jin, C. Ma, Q.-h. Zhang, L. Gu, C. Ge, J.-s. Wang, C. Wang, H.-z. Guo, and G.-z. Yang, Physical Review B **96**, 165206 (2017).

[78] X. Hao, Z. Wang, M. Schmid, U. Diebold, and C. Franchini, Physical Review B **91**, 085204 (2015).

[79] R. C. I. Matsushige, Japanese journal of applied physics **37**, 4539 (1998).

[80] P. Brüesch, *Phonons: Theory and experiments I: Lattice dynamics and Models of interatomic forces*, vol. 34 (Springer Science & Business Media, 2012).

[81] F. Jona and G. Shirane, *Ferroelectric crystals, international series of monographs on solid state physics* (Pergamon press Oxford, UK:, 1962).

[82] J. Nitta, T. Akazaki, H. Takayanagi, and T. Enoki, Physical Review Letters **78**, 1335 (1997).

[83] J. Lee, G. Schober, M. Bahramy, H. Murakawa, Y. Onose, R. Arita, N. Nagaosa, and

Y. Tokura, Physical review letters **107**, 117401 (2011).

[84] J. Sinova, D. Culcer, Q. Niu, N. Sinitsyn, T. Jungwirth, and A. H. MacDonald, Physical review letters **92**, 126603 (2004).

[85] V. M. Edelstein, Solid State Communications **73**, 233 (1990).

[86] K. Arii, M. Koshino, and T. Ando, Physical Review B **76**, 045311 (2007).

[87] A. Manchon and S. Zhang, Physical Review B **78**, 212405 (2008).

[88] A. Chernyshov, M. Overby, X. Liu, J. K. Furdyna, Y. Lyanda-Geller, and L. P. Rokhinson, Nature Physics **5**, 656 (2009).

[89] I. Mihai Miron, G. Gaudin, S. Auffret, B. Rodmacq, A. Schuhl, S. Pizzini, J. Vogel, and P. Gambardella, Nature materials **9**, 230 (2010).

[90] S. D. Ganichev, E. Ivchenko, V. Bel'Kov, S. Tarasenko, M. Sollinger, D. Weiss, W. Wegscheider, and W. Prettl, Nature **417**, 153 (2002).

[91] E. Bauer, G. Hilscher, H. Michor, C. Paul, E.-W. Scheidt, A. Gribanov, Y. Seropegin, H. Noël, M. Sigrist, and P. Rogl, Physical review letters **92**, 027003 (2004).

[92] P. Anderson, Physical Review B **30**, 4000 (1984).

[93] C. Tsuei and J. Kirtley, Reviews of Modern Physics **72**, 969 (2000).

[94] S. Yip, Physical Review B **65**, 144508 (2002).

[95] K. Samokhin, E. Zijlstra, and S. Bose, Physical Review B **69**, 094514 (2004).

[96] P. Frigeri, D. Agterberg, A. Koga, and M. Sigrist, Physical review letters **92**, 097001 (2004).

[97] I. Sergienko and S. Curnoe, Physical Review B **70**, 214510 (2004).

[98] B. Monserrat and D. Vanderbilt, Physical Review Materials **1**, 054201 (2017).

[99] M. A. Green and M. J. Keevers, Progress in Photovoltaics: Research and applications **3**, 189 (1995).

[100] B. W. Baugher, H. O. Churchill, Y. Yang, and P. Jarillo-Herrero, Nano letters **13**, 4212 (2013).

[101] A. Drozdov, M. Eremets, I. Troyan, V. Ksenofontov, and S. I. Shylin, Nature **525**, 73 (2015).

[102] A. D. Wright, C. Verdi, R. L. Milot, G. E. Eperon, M. A. Pérez-Osorio, H. J. Snaith, F. Giustino, M. B. Johnston, and L. M. Herz, Nature communications **7**, 1 (2016).

[103] D. Mou, R. Jiang, V. Taufour, R. Flint, S. Bud'ko, P. Canfield, J. Wen, Z. Xu, G. Gu,

and A. Kaminski, Physical Review B **91**, 140502 (2015).

[104] J. Schrieffer, Inc., New York (1964).

[105] W. Kohn, Physical Review Letters **2**, 393 (1959).

[106] J. Noffsinger, F. Giustino, B. D. Malone, C.-H. Park, S. G. Louie, and M. L. Cohen, Computer Physics Communications **181**, 2140 (2010).

[107] R. Peierls and R. E. Peierls, *Quantum theory of solids* (Oxford University Press, 1955).

[108] K. Page, T. Kolodiazhnyi, T. Proffen, A. K. Cheetham, and R. Seshadri, Physical review letters **101**, 205502 (2008).

[109] M. L. Cohen and S. G. Louie, *Fundamentals of condensed matter physics* (Cambridge University Press, 2016).

[110] A. Shevelkov, E. Dikarev, R. Shpanchenko, and B. Popovkin, Journal of Solid State Chemistry **114**, 379 (1995).

[111] F. Giustino, M. L. Cohen, and S. G. Louie, Physical Review B **76**, 165108 (2007).

[112] S. Poncé, E. R. Margine, C. Verdi, and F. Giustino, Computer Physics Communications **209**, 116 (2016).

[113] M. S. Bahramy and N. Ogawa, Advanced Materials **29**, 1605911 (2017).

[114] X. He, K.-j. Jin, H.-z. Guo, and C. Ge, Physical Review B **93**, 174110 (2016).

[115] W. McMillan, Physical Review **167**, 331 (1968).